Atlas of *Plasmodium falciparum* intraerythrocytic development using expansion microscopy

Benjamin Liffner[1*], Ana Karla Cepeda Diaz[2,3*], James Blauwkamp[1], David Anaguano[4,5], Sonja Frölich[6], Vasant Muralidharan[4,5], Danny W. Wilson[6,7,8], Jeffrey Dvorin[3,9], Sabrina Absalon[1#]

[1]Department of Pharmacology and Toxicology, Indiana University School of Medicine, Indianapolis, IN, USA.

[2]Biological and Biomedical Sciences, Harvard Medical School, Boston MA, USA.

[3]Division of Infectious Diseases, Boston Children's Hospital, Boston MA, USA.

[4]Center for Tropical and Emerging Global Diseases, University of Georgia, Athens, GA, USA.

[5]Department of Cellular Biology, Franklin College of Arts and Sciences, University of Georgia, Athens, GA, USA.

[6]Research Centre for Infectious Diseases, School of Biological Sciences, University of Adelaide, Adelaide, SA, Australia.

[7]Institute for Photonics and Advanced Sensing, University of Adelaide, Adelaide, SA, Australia.

[8]Burnet Institute, 85 Commercial Road, Melbourne, VIC, Australia.

[9]Department of Pediatrics, Harvard Medical School, Boston, MA, USA.

*These authors contributed equally

[#] Corresponding author

E-mail: Sabsalon@iu.edu

ABSTRACT

Apicomplexan parasites exhibit tremendous diversity in much of their fundamental cell biology, but study of these organisms using light microscopy is often hindered by their small size. Ultrastructural expansion microscopy (U-ExM) is a microscopy preparation method that physically expands the sample ~4.5x. Here, we apply U-ExM to the human malaria parasite *Plasmodium falciparum* during the asexual blood stage of its lifecycle to understand how this parasite is organized in three-dimensions. Using a combination of dye-conjugated reagents and immunostaining, we have catalogued 13 different *P. falciparum* structures or organelles across the intraerythrocytic development of this parasite and made multiple observations about fundamental parasite cell biology. We describe that the outer centriolar plaque and its associated proteins anchor the nucleus to the parasite plasma membrane during mitosis. Furthermore, the rhoptries, Golgi, basal complex, and inner membrane complex, which form around this anchoring site while nuclei are still dividing, are concurrently segregated and maintain an association to the outer centriolar plaque until the start of segmentation. We also show that the mitochondrion and apicoplast undergo sequential fission events while maintaining an association with the outer centriolar plaque during cytokinesis. Collectively, this study represents the most detailed ultrastructural analysis of *P. falciparum* during its intraerythrocytic development to date, and sheds light on multiple poorly understood aspects of its organelle biogenesis and fundamental cell biology.

IMPACT STATEMENT

Using ultrastructure-expansion microscopy we explore the fundamental cell biology of malaria parasites, providing new insights into processes including establishment of cell polarity and organelle fission.

INTRODUCTION

The human malaria parasite *Plasmodium falciparum* has a complex lifecycle that involves both human and mosquito hosts. Of its many lifecycle stages, the asexual replication of *P. falciparum* inside human red blood cells (RBCs) is responsible for the clinical symptoms of malaria. This asexual blood stage starts when a merozoite invades a host RBC and transitions through several morphologies before forming approximately 30 new daughter merozoites (Rudlaff, Kraemer, Marshman, & Dvorin, 2020) which egress from their host cell and invade new RBCs (Figure 1a). Host RBCs are approximately 7-8 µm in diameter (Kinnunen, Kauppila, Karmenyan, & Myllylä, 2011) and contain dozens of parasites, each with their own sets of organelles and structures. The small size of *P. falciparum* and its organelles still poses a challenge to the study of many facets of *P. falciparum* cell biology, especially when immunostaining is required.

Expansion microscopy is a set of sample preparation techniques that isotropically increase the physical size of a microscopy sample(Wassie, Zhao, & Boyden, 2019). While many expansion microscopy methods have been developed, ultrastructure expansion microscopy (U-ExM) (Gambarotto et al., 2019) was the first used in *Plasmodium* and since has been used in *P. falciparum* and across multiple apicomplexan parasites (Bertiaux et al., 2021; Dave, LaFavers, & Arrizabalaga, 2022; Liffner & Absalon, 2021; Oliveira Souza, Jacobs, Back, Bradley, & Arrizabalaga, 2022; R. Rashpa & Brochet, 2022; Severo et al., 2022). U-ExM results in the ~4.5 fold isotropic expansion of the sample and largely preserves its proteome, making it compatible with antibody staining and many fluorescent dyes (Gambarotto et al., 2019). The increase in physical sample size results in a dramatic increase in the ability to identify and distinguish different parasite structures. Thus, some structures that could previously only be investigated using electron microscopy can now be studied with the flexibility, scalability, and inexpensive nature of conventional light microscopy.

Application of U-ExM to *Plasmodium*, and other Apicomplexa, has already enhanced our understanding of parasite cell biology tremendously, resulting in the identification of new parasite structures and better characterization of the size and shape of others (Bertiaux et al., 2021; Liffner & Absalon, 2021; Qian et al., 2022; R. Rashpa & Brochet, 2022; Simon et al., 2021; Tomasina et al., 2022; Tosetti et al., 2020). Its significant impact on the field in such a short amount of time indicates U-ExM will be a technique heavily used in both *Plasmodium* and Apicomplexa more broadly for the foreseeable future. Considering

this, we set out to image *P. falciparum* structures and organelles across the asexual blood stage of the lifecycle to serve as a reference for the expanding number of U-ExM users who study Apicomplexa and to uncover previously invisible aspects of the cell biology of *P. falciparum*.

RESULTS

Ultrastructure Expansion Microscopy (U-ExM) reveals multiple parasite structures without the use of antibodies.

Dyes that are not antigen-specific are commonplace in light microscopy. N-hydroxysuccinimide (NHS) esters conjugated to dyes are amino-reactive and can be used for fluorescent labelling of protein density(Nanda & Lorsch, 2014). Similarly, BODIPY TR ceramide (BODIPY TRc) and other dye-conjugated fatty acids are commonly used for labelling lipids(Marks, Bittman, & Pagano, 2008). Coupling U-ExM with these dyes has already revealed parasite structures for which specific antibodies did not exist (Bertiaux et al., 2021; Liffner & Absalon, 2021; Simon et al., 2021). While antibody-based labelling provides high-specificity, this labelling lacks complexity and is limited to the specific protein or antigen that is being targeted. The more general stains increase the number of parasite features or organelles we can observe in the same sample without additional antibody markers. Therefore, these general stains allow for low-specificity but high-complexity imaging. An example of this principle is the use of uranyl acetate in electron microscopy to increase contrast by increasing the electron density of phosphate-rich structures in the cell (Rudlaff et al., 2020). While NHS esters and uranyl acetate can bring out similar features in the cell, they do not have the same reactivity and are therefore not equivalent stains. To better profile the subcellular organization of *P. falciparum* during the asexual blood stages, we set out to determine what parasite structures could, and could not, be visualised by U-ExM when using some of these dyes.

We, and others, have previously shown that combining BODIPY TRc and dye-conjugated NHS ester with U-ExM allows visualisation of the parasite plasma membrane (PPM), parasitophorous vacuolar membrane (PVM), nuclear envelope, rhoptries, endoplasmic reticulum, centriolar plaque, basal complex,

101 and apical polar rings (APRs) (Bertiaux et al., 2021; Liffner & Absalon, 2021; Simon et al., 2021). However,
102 many important organelles and parasite structures are either not identifiable using these stains or have yet to
103 be validated, including the mitochondrion, apicoplast, and cytostomes.

104 To identify and validate the location of as many parasite organelles and structures as possible, we
105 utilized U-ExM coupled with BODIPY TRc, Alexa Fluor 405-conjugated NHS ester (which we will refer to
106 as "NHS ester"), the nucleic acid (i.e., DNA) stain SYTOX Deep Red, and antibodies directed against 13
107 different subcellular targets (microtubules, centriolar plaque, basal complex, IMC, mitochondrion,
108 apicoplast, cytostome, rhoptry bulb, rhoptry neck, micronemes, cytoplasm, endoplasmic reticulum, and
109 Golgi). In this study all parasites were fixed in 4% paraformaldehyde (PFA), unless otherwise stated, and
110 anchored overnight at 37 °C before gelation, denaturation at 95 °C and expansion. Expanded gels were
111 measured, before shrinking in PBS, antibody staining, washing, re-expansion, and imaging (Figure 1b).
112 Parasites were harvested at multiple time points during the intraerythrocytic asexual stage and imaged using
113 Airyscan2 super-resolution microscopy, providing high-resolution three-dimensional imaging data (Figure
114 1c). A full summary of all target-specific stains used in this study can be found in Figure 1d.

115 The first protein we imaged was aldolase, a marker of the parasite cytoplasm (Figure 1 – Figure
116 Supplement 2). Aldolase staining was present in all asexual replication stages. During the ring stage, the
117 "ameboid" shape of the parasite is readily visualized, consistent with previous studies of this stage in time-
118 lapse microscopy of live parasites (Grüring et al., 2011) (Figure 1 – Figure Supplement 2). Regions within
119 the parasite where both aldolase and NHS ester staining were absent are consistent with the expected area of
120 the food vacuole. Typically, the food vacuole would be filled with hemozoin, however, this crystal likely
121 cannot expand and therefore leaves a large space inside the parasite that does not contain significant protein
122 density (Figure 1 – Figure Supplement 2).

123 **The centriolar plaque (CP), nuclear microtubule organizing center (MTOC) and microtubules.**

124 The first major transition during the blood stage of the lifecycle occurs when the parasites turn from
125 rings into trophozoites. Soon after this transition, the parasite will begin to replicate its DNA and undergo
126 mitosis followed by nuclear fission (Gerald, Mahajan, & Kumar, 2011). Mitosis is coordinated by
127 microtubules, which are in turn nucleated by structures called microtubule organizing centers (MTOCs)

(Sanchez & Feldman, 2017). *P. falciparum* has a structure known as the centriolar plaque (CP) that spans the nuclear envelope, with intranuclear and cytoplasmic portions (Simon et al., 2021). In this study we will refer to the intranuclear portion of the CP as the inner CP, and the cytoplasmic portion of the CP as the outer CP. The inner CP acts as the nuclear MTOC that coordinates *P. falciparum* mitosis, while the function of the outer CP is unknown in asexual blood-stage parasites. The most commonly used MTOC markers are the centrins, which in *Plasmodium* comprise four proteins that localize to the outer CP and appear after intranuclear microtubules have already formed (Simon et al., 2021). Given that an MTOC is required for microtubule formation, this implies that an MTOC forms before centrin is visible. To investigate these processes in more detail, we visualized the biogenesis and dynamics of the centriolar plaque and microtubules during the trophozoite and schizont stages by pairing NHS ester, which we have recently shown can stain both the inner and outer CP (Liffner & Absalon, 2021), with an anti-centrin antibody (Clone 20H5, raised against centrin from *Chlamydomonas*) (Figure 2a). This antibody likely recognizes centrin 3 in *P. falciparum* (Mahajan et al., 2008), but a recent study suggests that all four *P. falciparum* centrins share an outer CP localization (Voß, Klaus, Ganter, & Guizetti, 2022).

Centriolar plaque biogenesis and disassembly

Neither a recognizable centriolar plaque nor above-background centrin staining were observed in ring-stage parasites (Figure 2b) (Simon et al., 2021). The inner CP first appeared in mononucleated trophozoites but changed morphology as these parasites got closer to their first nuclear division. In the 23 mononucleated trophozoites we imaged, 52% of centriolar plaques lacked cytoplasmic extensions (Figure 2 – Figure Supplement 1a&b). These centriolar plaques contained only had the inner CP, lacking the outer CP as observed by NHS ester (Figure 2a&b). All 12 of the trophozoites with an inner CP but no outer CP also lacked centrin staining (Figure 2 – Figure Supplement 1c). This matches previous reports that centrin is specifically associated with the outer CP (Simon et al., 2021). As expected, this early centriolar plaque lacking the outer CP was capable of nucleating microtubules (Figure 2 – Figure Supplement 1a). The centrin focus and outer CP became visible in mononucleated trophozoites after nucleation of the intranuclear microtubules but prior to the first centriolar plaque duplication event of the first mitosis (Figure 2 – Figure Supplement 1a), consistent with previous reports (Simon et al., 2021). The cytoplasmic extensions that form

155 the outer CP began at the nuclear membrane and ended at an NHS ester-dense focus located at the parasite
156 plasma membrane (PPM) (Figure 2b). This association between the outer CP and the PPM has previously
157 been observed in gametocytes and asexual blood stages (Li et al., 2022; Ravish Rashpa, Klages, Schvartz,
158 Pasquarello, & Brochet, 2023), but the temporal nature of this association during the asexual blood stages
159 remained uncharacterized. Our observation of the outer CP using NHS ester, discussed further below,
160 combined with the temporal pattern of outer CP-PPM association suggests that nuclei are physically
161 anchored to the PPM while parasites are undergoing mitosis.

162
163 For as long as parasites continue to undergo mitosis throughout schizogony, the outer CP remains in
164 contact with the PPM (Figure 2a). The outer CP appears as one or two elongated bundles, referenced
165 throughout this paper as 'branches', that stain densely with NHS ester. These branches showed one or two
166 centrin foci that largely matched branch number. That is, of the 139 single-branched outer CPs (outer CPs
167 with a single cytoplasmic extension branch) observed, all had a single centrin focus, and of the 30 double-
168 branched outer CPs observed, 92% had two centrin foci (Figure 2b; Figure 2 – Figure Supplement 1c). The
169 overwhelming coordination between number of cytoplasmic extension branches and number of centrin foci
170 suggests centrin duplication and duplication of the branches of the outer CP happens quickly and
171 simultaneously. The few cases when there is a mismatch between the number of cytoplasmic extensions and
172 centrin foci all occur in double-branched outer CPs and can be attributed to limitations in our ability to
173 resolve two centrin foci (Figure 2 – Figure Supplement 1c&d).

174 The relative abundance of nuclei with a single centriolar plaque, defined as a centriolar plaque not
175 forming a mitotic spindle, versus mitotic centriolar plaques, centriolar plaques anchored to a mitotic spindle,
176 varied throughout schizogony as did their branch numbers (Figure 2 – Figure Supplement 1). As we
177 previously observed that the inner CP forms first, we hypothesized that centriolar plaques start out without
178 an inner CP and then develop a single cytoplasmic extension and centrin focus which duplicate ahead of
179 centriolar plaque duplication and then segregate with each centriolar plaque during miotic spindle formation
180 and karyokinesis (Figure 2b). This means that during the rapid mitotic events of schizogony that take place
181 at the 6-12 nuclei stage, single outer CPs with a single cytoplasmic extension are very rare. We observed

182 them in just 6% of 221 imaged centriolar plaques (Figure 2 – Figure Supplement 1b). Single outer CPs with
183 a single cytoplasmic extension were only abundant when the pace of nuclear replication was slow at the
184 early schizont stage (24% of 76 centriolar plaques imaged in cells with 2-5nuclei) and the end of
185 segmentation (44% of 290 centriolar plaques imaged in segmenting parasites).

186 This observed pattern of duplication and segregation also suggests that double-branched outer CPs
187 with two centrin foci have committed to undergoing a new round of mitosis and that the duplication of
188 cytoplasmic extensions represents the first identifiable step in centriolar plaque duplication. In line with this
189 hypothesis, the most common centriolar plaque states in schizonts prior to segmentation are single centriolar
190 plaques with 2 cytoplasmic extensions (26% of centriolar plaques in cells with 2-5 nuclei, 52% in cells with
191 6-12 nuclei) which have committed to the next round of mitosis and mitotic centriolar plaques with one
192 extension each (42% of centriolar plaques in cells with 2-5 nuclei, 36% in cells with 6-12 nuclei) which are
193 finishing a round of mitosis. Interestingly, 8% of centriolar plaques observed in the 2-5 nuclei stage and 6%
194 in the 6-12 nuclei stage were mitotic and double-branched, suggesting the duplication of cytoplasmic
195 extensions, and commitment to the next round of mitosis, can happen before karyokinesis is completed
196 (Figure 2 – Figure Supplement 1e; Figure 2 – Figure Supplement 2).

197 Outer CP branch number reaches semi-synchrony at the beginning of segmentation as defined by the
198 first appearance of a basal complex by NHS ester. At this point, rather than seeing a variety of centriolar
199 plaque states and branch numbers, virtually all centriolar plaques in the same cell share the same mitotic
200 state and branch number. Most centriolar plaques are mitotic with a single cytoplasmic extension during
201 early segmentation and then appear as single centriolar plaque with a single extension during mid-
202 segmentation (Figure 2 – Figure Supplement 1b). By the time segmentation is completed, the centriolar
203 plaque is no longer visible by NHS ester, suggesting that it may disassemble after all mitotic events are
204 finished (Figure 2b; Figure 2 – Figure Supplement 1b). To ensure imaged parasites were fully segmented,
205 we arrested parasite development by adding the reversible protein kinase G inhibitor Compound 1 (C1)
206 (Collins et al., 2013; Gurnett et al., 2002; H. M. Taylor et al., 2010). This inhibitor arrests parasite
207 maturation after the completion of segmentation but before egress. When C1 is washed out, parasites egress
208 and invade normally, ensuring that observations made in C1-arrested parasites are physiologically relevant

and not a developmental artefact due to arrest. Of 159 nuclei imaged in 6 C1-arrested schizonts, none showed the presence of a centriolar plaque.

The apical polar rings, Golgi, and rhoptries are all segregated with the centriolar plaque.

Given the cytoplasmic coordination of mitotic events and the physical tethering of the nucleus to the PPM throughout schizogony, we investigated whether we could observe any coordination extending to the apical organelles and other structures known to be present near the centriolar plaque at these stages. We observed close association between the outer CP and the rhoptries, Golgi, basal complex, and an apical density reminiscent of the APR.

The number of basal complex structures closely matched the number of outer CP extensions throughout schizogony (156 observed cytoplasmic extensions, 153 observed basal complexes). The basal complex, discussed in detail below, appears as a ring-like structure from early schizogony to the completion of segmentation. No basal complex structures were observed in centriolar plaques without cytoplasmic extensions. Of 82 single-branched outer CPs imaged, 81 (99%) showed a single basal complex structure. Of 37 double-branched outer CPs imaged, 33 (89%) showed two basal complex structures. As we observed when imaging centrin foci, the few cases when there is a mismatch between the number of cytoplasmic extensions and basal complex structures mostly occur in double-branched outer CPs. However, in this case, the mismatch cannot be attributed to resolution and most likely reflects a transition state in basal complex replication. CINCH stains the basal complex in a punctate pattern until early segmentation, allowing us to visualize basal complex division events as gaps in the punctate staining (Figure 4b). The occasional presence of two cytoplasmic extensions in the absence of these gaps suggests that basal complex division, when visualized by breaks in CINCH staining, is less simultaneous with outer CP branch duplication than centrin focus duplication.

Rhoptry biogenesis, discussed further below, was also closely tied to the number and position of the outer CP. This association of one rhoptry per branch, however, is broken at the start of segmentation, when 205 of 211 imaged centriolar plaques (97%) had a rhoptry pair per outer CP branch. Further suggestive of centriolar plaque-rhoptry interaction is the fact that the rhoptries were positioned immediately next to the

235 outer CP for as long as these were visible by NHS ester. While we had no APR protein marker, the
236 cytoplasmic extensions always ended in an NHS ester-dense focus at the plasma membrane. At the
237 beginning of segmentation, this focus obtained a morphology suggestive of the APR based on its ring shape,
238 position, and size. As described above, a small percentage of parasites commit to the next round of mitosis
239 before they finish segregating their genetic material. In these parasites, centriolar plaque-associated
240 organelles continued to match the number of cytoplasmic extensions. This gave rise to nuclei that were
241 anchored to four basal complexes, four single rhoptries, and four proto-APR densities in close proximity
242 (Figure 4 – Figure Supplement 1). This matches previous observations by three-dimensional electron
243 microscopy that a single nucleus can have 4 sets of apical buds (Rudlaff et al., 2020).

244 We also characterized the distribution of the Golgi and its location near the centriolar plaque and
245 apical organelles, this spatial correlation had been previously described by electron microscopy but has not
246 been thoroughly explored (Bannister, Hopkins, Fowler, Krishna, & Mitchell, 2000). The Golgi was
247 visualised using an antibody to ER lumen protein retaining receptor 2 (ERD2), a cis-Golgi marker expressed
248 throughout intraerythrocytic development (H. G. Elmendorf & K. Haldar, 1993) (Figure 2 – Figure
249 Supplement 2). Small regions of Golgi were visible at all development stages. In ring-stage parasites and
250 mononucleated trophozoites, one or two Golgi foci were observed near the nucleus but had no clear
251 proximity to the centriolar plaque. In all 5 imaged parasites with less than 2 nuclei and an outer CP, no Golgi
252 was observed near the inner CP. In parasites that had undergone the first round of mitosis and had an outer
253 CP, the Golgi was proximal to the extensions of the outer CP (Figure 2 – Figure Supplement 1b & 2) and
254 closely matched their number and presence. Specifically, 21 of 22 imaged parasites with visible outer CPs
255 had Golgi staining near each branch of their outer CP (Figure 2 – Figure Supplement 1b). While increased
256 Golgi-centriolar plaque proximity coincides with the appearance of the cytoplasmic extensions, the Golgi is
257 able to remain towards the apical end of the parasite after these tethers and the centriolar plaque are no
258 longer visible by NHS ester. However, at this point the Golgi loses its close proximity to the apical
259 organelles and is situated closer to the nucleus. In C1-arrested schizonts, each merozoite has a single Golgi
260 that remains at the apical end of the parasite, typically between the rhoptry bulb and the nucleus (Figure 2 –
261 Figure Supplement 2).

In contrast, we did not observe a centriolar plaque association in the distribution of the endoplasmic reticulum (ER) (Figure 4 – Figure Supplement 2) within the parasite. The ER was visualised using an antibody to Binding Immunoglobulin Protein (BIP), a constitutively expressed ER lumen protein (Kumar, Koski, Harada, Aikawa, & Zheng, 1991). As expected, ER was detected at all stages of intraerythrocytic development (Figure 4 – Figure Supplement 2). In ring-stage and mononucleated trophozoite-stage parasites, the ER could be seen wrapping around the nucleus and forming recognizable cisternae. In multinucleated parasites, the ER was too dense to observe cisternae, but large regions of the cell were occupied by the ER. Following segmentation in C1-arrested schizonts, the ER was only observed contiguous with the nuclear envelope.

Combining the observations that the centriolar plaque is physically tethered to the PPM through the outer CP and that this anchoring is closely associated with organelles that will define the apical end of the parasite (Golgi, rhoptries, basal complex, and apical polar rings), we suggest that this tethering by the outer CP establishes apical-basal polarity in the parasite early in schizogony. Considering that rhoptries are formed from Golgi-derived cargo (Ben Chaabene, Lentini, & Soldati-Favre, 2021; Counihan, Kalanon, Coppel, & de Koning-Ward, 2013), it is unsurprising to find the Golgi forms part of this apical cluster of organelles throughout schizogony. The confined space between nuclear envelope and PPM that these organelles are packed into, for example, may allow each nucleus to provide rhoptry cargo locally to their own rhoptries rather than to all rhoptries in the cell. The same principle could apply to other apical Golgi-derived organelles. However, it remains unclear what role, if any, the outer CP plays in this association, whether any organelles besides the nucleus are physically tethered by these extensions, and how these clusters of organelles remain together during the rapid mitotic events constantly separating sister centriolar plaques.

Characterisation of intranuclear microtubules.

P. falciparum asexual blood stages are known to have two classes of microtubules; intranuclear microtubules that partake in mitosis (Liffner & Absalon, 2021; Simon et al., 2021), and subpellicular microtubules (SPMTs) that are cytosolic and extend in a single spine from the apical end of merozoites (Liffner & Absalon, 2021; Simon et al., 2021). Investigating microtubules with an anti-α-tubulin antibody,

289 we failed to detect microtubules in ring-stage parasites, consistent with previous observations (Figure 3 –
290 Figure Supplement 1) (Simon et al., 2021). Intranuclear microtubules were first visible in mononucleated
291 trophozoite-stage parasites and were present until early segmentation stages, with no intranuclear
292 microtubules visible by the end of segmentation (Figure 3a). Intranuclear microtubules arrange into three
293 distinct spindle structures: hemispindles, mitotic spindles, and interpolar spindles. Hemispindles are
294 microtubule structures coming from a single centriolar plaque that retract prior to centriolar plaque
295 duplication. Mitotic spindles appear following centriolar plaque duplication and separate sister chromatids
296 during mitosis. When the two centriolar plaques migrate away from each other, they remain connected by an
297 elongated microtubule structure called the interpolar spindle (or elongated spindle), which retracts prior to
298 nuclear fission (Liffner & Absalon, 2022; Machado, Klaus, Klaschka, Guizetti, & Ganter, 2022; Simon et al.,
299 2021). It has recently been shown that the interpolar spindle is short-lived relative to the hemispindle and
300 mitotic spindle (Machado et al., 2022; Simon et al., 2021). In this study, we observed 24 interpolar spindles,
301 which allowed us to perform the first detailed characterisation of this spindle type (Figure 3b).

302 Interpolar spindles have microtubule branches that connect the two distant centriolar plaques
303 (interpolar microtubules), and microtubule branches that do not connect the centriolar plaques (non-
304 interpolar microtubules). Each interpolar spindle contained an average of 12.5 (± 2.6 SD) total microtubules,
305 of which 1.3 (± 0.6 SD) were interpolar microtubules and 11.2 (± 2.8 SD) were non-interpolar microtubules
306 (Figure 3c). The average number of non-interpolar branches per inner CP was 5.6, which is similar to the
307 previously reported average number of branches in a hemispindle of 5 to 6 (Liffner & Absalon, 2021; Simon
308 et al., 2021). This suggests that only the interpolar microtubules retract during the interpolar spindle to
309 hemispindle transition. We measured interpolar microtubules in 3D, adjusting for expansion factor by
310 dividing the measured distance by 4.25, the median expansion factor observed in this study (Figure 1 –
311 Figure Supplement 1; Materials and Methods). All of the following measurements in this study are reported
312 in this expansion-corrected format. Interpolar microtubules ranged from ~1-5 µm, with a mean length of 2.9
313 µm (± 1.0 µm SD) or 12.47 µm before expansion factor correction (Figure 3d). In all cases, the centriolar
314 plaques connected by interpolar spindles were anchored to the plasma membrane by their cytoplasmic
315 extensions. The large variability in interpolar microtubule size and the continued tethering of the outer CPs

to the PPM suggest that interpolar microtubules push PPM-anchored centriolar plaques to opposite sides of the cell without causing detachment from the PPM. It is unclear how parasites achieve this sliding effect or how centriolar plaque-associated organelles are able to retain this association while centriolar plaques are moved large distances.

Subpellicular microtubule length and biogenesis.

Subpellicular microtubules are nucleated in the cytoplasm and have long been observed in merozoites (Aikawa 1967). SPMTs have been shown to be stabilised by polyglutamylation (Bertiaux et al., 2021) and can be identified specifically using a combination of anti-tubulin and anti-PolyE antibodies (Figure 3e). Using this approach, we characterised 86 SPMTs in 50 merozoites from C1-arrested schizonts. These nascent merozoites had between 1 and 3 SPMTs, with an average of 1.7 (± 0.6 SD) (Figure 3f). Of 50 imaged merozoites, 48 had at least one SPMT that extended >50% of cell length from the apical polar ring to the basal complex. This longest microtubule in a merozoite had an average length of 1.01 µm (± 0.24 µm SD). In merozoites with more than one SPMT, the second and third microtubules were shorter than the first, having an average length of 0.8 µm (± 0.21 µm SD). Given the large variation in SPMT size and observation that, in segmenting schizonts, the basal end of the SPMTs was in contact with the basal complex throughout segmentation, we hypothesise that most SPMTs measured in our C1-treated schizonts had partially depolymerised. *P. falciparum* microtubules are known to rapidly depolymerise during fixation (Liffner & Absalon, 2022; Simon et al., 2021). It is unclear, however, why this depolymerization was observed most often in C1-arrested parasites. Thus, we cannot determine whether these shorter microtubules are a by-product of drug-induced arrest or a biologically relevant native state that occurs at the end of segmentation.

Little is known about SPMT biogenesis during the asexual blood stage of *P. falciparum*, but it is currently hypothesized that they are nucleated by the apical polar rings (Hanssen et al., 2013; Morrissette & Sibley, 2002), as is the case in *Toxoplasma* (Morrissette & Sibley, 2002; Tran et al., 2010). Curiously, TgCentrin 2 localizes to the apical polar ring of *Toxoplasma* tachyzoites (K. Hu, 2008), but no Centrin 2 has been observed to localize to the apical polar rings of *P. falciparum*. Furthermore, it was recently shown that the SPMTs of *P. falciparum* gametocytes, which lack an APR, are formed at the outer CP, in the space between the nuclear envelope and PPM (Li et al., 2022). Leveraging our ability to specifically detect SPMTs

using PolyE, we investigated the possibility that merozoite SPMTs are also formed at the outer CP and subsequently transferred onto the apical polar ring during segmentation. In schizonts where nuclei are approaching or have completed their final mitosis (~15n), we observed small cytoplasmic microtubules that stained strongly with PolyE appear in the area between the outer CP and PPM (Figure 3g). However, we did not achieve a resolution that allowed us to distinguish individual APRs or to confidently pinpoint whether the microtubules were nucleated at the APRs or the cytoplasmic extensions. Likely, higher resolution imaging techniques are needed to resolve the site of SPMT nucleation in merozoites.

Segmentation machinery (inner membrane complex and basal complex)

Following replication of their genetic material during the trophozoite and early schizont stages, parasites partition their nuclei and organelles into ~30 daughter merozoites from the common cytoplasm of a schizont (Francia & Striepen, 2014). This form of cytokinesis, called segmentation, takes place in the final hours of schizogony and culminates with the physical separation of each daughter cell and their egress from the host RBC. The inner membrane complex (IMC) is a double lipid bilayer formed from flattened vesicles that scaffolds the process of segmentation as well as anchors many proteins important for parasite shape and motility (Harding & Meissner, 2014).

The IMC cannot be distinguished from the plasma membrane by U-ExM

The IMC forms *de novo* during segmentation starting at the apical end of the parasite, where the outer CP is anchored to the plasma membrane (Figure 4 – Figure Supplement 1a) (Harding & Meissner, 2014). This can be observed using the IMC-anchored protein Glideosome associated protein 45 (GAP45), which bridges the IMC and plasma membrane, as well as using BODIPY TRc, which shows increased membrane staining in the area overlapping GAP45 (Jones, Kitson, & Rayner, 2006) (Figure 4 – Figure Supplement 1a). As segmentation progresses, the IMC expands around the nucleus and associated organelles until it envelops the daughter cell, leaving an opening at the apical end, where the apical polar ring is located, and the basal end, where the basal complex resides (Figure 4 – Figure Supplement 3a). While the pellicle was easily visualized as a whole, we were unable to distinguish the IMC membranes from the PPM (Figure 4 – Figure Supplement 3b&c). We stained parasites using the plasma membrane marker MSP1 and two

different IMC markers: GAP45, which lies between the IMC and PPM, and IMC1g, which is attached to the cytoplasmic face of the IMC (M. J. Blackman, T. J. Scott-Finnigan, S. Shai, & A. A. Holder, 1994; Cepeda Diaz, Rudlaff, Farringer, & Dvorin, 2023; Kono et al., 2012). In both cases we were unable to resolve the IMC marker from MSP1 (Figure 4 – Figure Supplement 3b&c).

Basal complex dynamics throughout segmentation

The basal complex is an essential ring structure located at the basal end of the IMC (Morano & Dvorin, 2021). It is hypothesized to act as a contractile ring that guides IMC biogenesis and mediates abscission of newly formed merozoites by separating the IMC and plasma membrane from the residual body. We used parasites where PfCINCH, a basal complex marker, was tagged with a spaghetti monster V5 (smV5) tag to follow basal complex development throughout schizogony (Figure 4a) (Rudlaff, Kraemer, Streva, & Dvorin, 2019). CINCH is first visible at early schizogony (3-5 nuclei stage) as a small ring-like structure surrounding an NHS ester-dense focus on the plasma membrane that is tethered to the centriolar plaque (Figure 4b). Of 55 early schizont centriolar plaques imaged, 44 (80%) had matching numbers of outer CP branches and basal complex structures. This suggests that as centriolar plaques divide, they each inherit a CINCH ring that has been split by the duplication of the cytoplasmic tethers (Figure 4b). Early IMC proteins have been described to form cramp-like structures like these prior to attaining their characteristic ring structure later in schizogony (G. Hu et al., 2010; Kono et al., 2012). During the rapid nuclear divisions of schizogony, 77% of the CINCH structures of mitotic centriolar plaques show a break in the ring (Figure 4 – Figure Supplement 1b). This break faces a sister basal complex with its own cytoplasmic extension (Figure 4b and Figure 4 -Figure Supplement 1b). These observations suggest that, upon duplication of the outer CP branches, the basal complex ring likely “breaks” into two semicircles which re-seal to form their own ring prior to the next branch duplication (Figure 4b, Figure 4 - Figure Supplement 1b).

Once segmentation begins and the outer CP stops duplicating, CINCH forms a *bona fide* ring with smooth borders (Figure 4). This matches previously reported behaviour of early IMC proteins and supports our hypothesis that the cramp-like structures arise from IMC and basal complex division. At this point, nuclei reach a point of semi-synchronicity. All 64 imaged centriolar plaques in early segmentation parasites had duplicated and were forming a mitotic spindle. This event marks the last nuclear division the parasite

will undergo. Each of these centriolar plaques had a single uninterrupted basal complex ring (Figure 4b). Thus, we cease to observe events where a single nucleus is attached to four basal complexes as centriolar plaques have ceased committing to future rounds of mitosis. As the parasite undergoes segmentation, the basal complex expands and starts moving in the basal direction. By the time the basal complex reaches its maximum diameter, all nuclear divisions have been completed, each nucleus has a single centriolar plaque and basal complex, and no mitotic spindles are visible (Figure 4). After this point, the basal complex contracts and continues to move away from the apical end. By the time segmentation is completed, the basal complex is an NHS ester dense ring that is smaller than the apical polar ring.

NHS ester as a basal complex marker

While the basal complex stains brightly with NHS ester at the end of segmentation (Figure 4), this staining is not consistent throughout schizogony. NHS-ester staining of the basal complex is not visible or is very faint during early schizogony. Once the basal complex attains its *bona fide* ring form during early segmentation, it stains reliably, though faintly, with NHS ester. This staining intensifies after the basal complex begins to contract. The denser staining observed during basal complex contraction could be due to recruitment of more basal complex proteins at the midpoint of schizogony, an increase in protein density as the ring area decreases during contraction, or both. Once the parasites finish segmentation, the basal complex is at its brightest (Figure 4b). While NHS ester staining correlates with CINCH, it does not perfectly overlap with it. CINCH consistently appears as a larger ring with a slight basal shift relative to NHS ester after the basal complex reaches maximum diameter, an effect most visible at the end of segmentation (Figure 4b). Since this shift is consistent with parasite anatomy regardless of parasite orientation, it suggests it is not an imaging artifact. There is no primary antibody against CINCH at this point, and so it is not possible to determine whether the lack of overlap with NHS ester is due to distance between the smV5 tag and the main protein density of CINCH (CINCH is 230kDa). It is also possible that this difference in localization reflects basal complex architecture similar to that previously observed in *Toxoplasma gondii*, where the basal complex consists of multiple concentric rings (Anderson-White et al., 2012; Engelberg, Bechtel, Michaud, Weerapana, & Gubbels, 2022; K. Hu, 2008; Roumégous et al., 2022).

Mitochondrion and apicoplast

The apicoplast and mitochondrion undergo pronounced morphological changes during the *P. falciparum* blood-stage lifecycle (van Dooren et al., 2005; van Dooren, Stimmler, & McFadden, 2006). Both are long, and often branching, organelles whose complex three-dimensional morphologies have only been robustly studied using electron microscopy-based techniques(Rudlaff et al., 2020).

Looped regions of the mitochondrion display low membrane potential.

To visualize the mitochondria, we stained live parasites using Mitotracker Orange CMTMRos prior to fixation and expansion (Figure 5 – Figure Supplement 1a). Mitotracker Orange CMTMRos accumulates in live mitochondria, driven electrophoretically by membrane potential, and is retained after fixation(Elmore, Nishimura, Qian, Herman, & Lemasters, 2004; Poot et al., 1996). When imaged at high resolution, Mitotracker can be used to observe individual cristae in the mitochondria of mammalian cells(Wolf et al., 2019). *Plasmodium* cristae morphology is different from that found in mammalian mitochondria; cristae are thought to be bulbous or tubular rather than lamellar and are present in gametocytes but absent from asexual blood-stage parasites(Evers et al., 2021; Evers et al., 2023). To our surprise, rather than showing continuous staining of the mitochondria, Mitotracker staining of our expanded parasites revealed alternating regions of bright and dim staining that formed Mitotracker-enriched pockets (Figure 5 – Figure Supplement 1b). These clustered areas of Mitotracker staining were highly heterogeneous in size and pattern. Small staining discontinuities like these are commonly observed in mammalian cells when using Mitotracker dyes due to the heterogeneity of membrane potential from cristae to cristae as well as due to fixation artifacts. At this point, we cannot determine whether the staining we observed represents a true biological phenomenon or an artefact of this sample preparation approach. Our observed Mitotracker-enriched pockets could be an artifact of PFA fixation, a product of local membrane depolarization, a consequence of heterogeneous dye retention, or a product of irregular compartments of high membrane potential within the mitochondrion, to mention a few possibilities. Further research is needed to conclusively pinpoint an explanation.

In addition to these small staining discontinuities, we observed large gaps in Mitotracker staining within parasites at all stages of development. This included pre-segmentation parasites, where we would

expect a single continuous mitochondrion to be present (Figure 5 – Figure Supplement 1a). To our knowledge, no membrane potential discontinuities or fixation artifacts of this size have been reported in mammalian cells. So, as a secondary way to visualise the mitochondria and better characterize these staining discontinuities, we generated a transgenic cell line with the putative ATP synthase F0 subunit-d (ATPd, Pf3D7_0311800) tagged with a spaghetti monster HA tag(Viswanathan et al., 2015) (Figure 5 – Figure Supplement 2). ATPd is a membrane-embedded proton channel that had not previously been localized to the mitochondria in *P. falciparum* but was identified as a mitochondrial protein in a recent proteomics study(Esveld et al., 2021; Evers et al., 2021). Furthermore, its *Toxoplasma* homologue has been shown to localize to the mitochondria (Barylyuk et al., 2020; Sheiner et al., 2011). We confirmed that ATP synthase subunit F0 localizes to *P. falciparum* mitochondria, as it largely co-localized with Mitotracker staining, forming a border around it due to its membrane association (Figure 5 – Figure Supplement 1a). ATPd, like Mitotracker, had a heterogenous distribution throughout the mitochondria, but it did not show the same large gaps in staining. ATPd allowed us to better visualize regions of the mitochondria that appeared to fold onto themselves and fuse with each other, as has been previously described (van Dooren et al., 2005). Thus, Mitotracker and ATPd are both useful but imperfect markers for the mitochondria, with neither of them showing a continuous, even distribution throughout the organelle.

Curiously, 25 of 26 imaged parasites showed Mitotracker discontinuities specifically in regions where the ATPd signal formed looped structures (Figure 5b). These structures were defined as areas where the mitochondria showed a turn or fold of ~180°. Of the 41 looped regions identified, 75% lacked Mitotracker staining. This suggests that mitochondria looped regions in *P. falciparum* have some degree of depolarization that prevents Mitotracker accumulation or that Mitotracker initially accumulates in these regions but is not bound and retained. The biological significance of these areas, if any, is currently unclear.

Growth of the apicoplast and mitochondrion

To visualize the apicoplast, we utilized a previously established cell line that expresses GFP fused to the apicoplast transit peptide of acyl carrier protein (ACP) (Florentin, Stephens, Brooks, Baptista, & Muralidharan, 2020), which we will refer to as Apicoplast-GFP. This marker allowed for a relatively even and continuous staining of the organelle. We quantified mitochondrion and apicoplast signal area using

ATPd-smHA and Apicoplast-GFP respectively as a proxy measurement of size (Figure 5c&6b). Tracking this in parallel to parasite nucleus number allowed us to determine whether the growth of these organelles occurred progressively with simultaneous rounds of mitosis and nuclear division. In mononucleated ring and trophozoite parasites, both the mitochondria and the apicoplast are relatively small, having an average area of 13.39 μm^2 (± 15.1 μm^2 SD) and 4.81 μm^2 (± 2.62 μm^2 SD) respectively in expanded parasites (Figure 5c & 6b). As expected from live cell observations(van Dooren et al., 2005), both organelles show significant growth and spread throughout the cell in multinucleated parasites, adopting an elongated and branching morphology (Figure 5&6). Mitochondria grow almost exclusively during the first two rounds of nuclear replication, achieving an average size of 87.9 μm^2 (± 15.9 μm^2 SD) at the 2-5 nuclei stage. This size remains relatively constant until segmentation, with the average mitochondria size right before the start of fission being 99.6 μm^2 (± 37.4 μm^2 SD) (Figure 5c). In contrast, the apicoplast continues to grow past the 2-5 nuclei stage, having an average size of 25.5 μm^2 (± 7.21 μm^2 SD) at the 2-5 nuclei stage and 34.97 μm^2 (± 11.23 μm^2 SD) in cells with >15 nuclei (Figure 6b). These data suggest that the mitochondrion and apicoplast do not grow simultaneously with or as a response to nuclear replication during schizogony. Rather, both organelles show the largest increase in size during the 1 to 2 nuclei transition and either plateau in size, in the case of the mitochondria, or enter a second phase of slower growth that ends shortly before segmentation, in the case of the apicoplast.

Fission of the mitochondrion and apicoplast

P. falciparum has a single, large, branching, mitochondrion and apicoplast throughout most of the asexual blood stage (van Dooren et al., 2005; van Dooren et al., 2006; Verhoef, Meissner, & Kooij, 2021). During segmentation, however, these organelles undergo fission such that each merozoite inherits an individual apicoplast and mitochondrion (Rudlaff et al., 2020; van Dooren et al., 2005). While it has been shown that apicoplast fission occurs before mitochondrial fission, it is unclear how fission occurs(Rudlaff et al., 2020). A recent review (Verhoef et al., 2021) posed three possible mechanisms: synchronous fission where the organelle simultaneously divides into all daughter parasites at once, outside-in fission where fission occurs at the ends of the organelle, or branching point fission where a first fission event divides the organelle into larger segments and a subsequent fission event leaves each merozoite with an individual

organelle (Verhoef et al., 2021). It also remains unclear how accurate segregation into daughter cells is monitored. In *T. gondii*, the apicoplast associates with the centrosomes prior to undergoing fission. A similar association between apicoplasts and centriolar plaques has been proposed in *Plasmodium* but still lacks evidence due to the difficulty of observing the *Plasmodium* centriolar plaque in live cells (van Dooren et al., 2005). The mitochondrion is not thought to associate with the centriolar plaque in *Toxoplasma* or *Plasmodium* and its mechanism for ensuring accurate segregation remains unknown.

In the process of imaging the mitochondria and apicoplasts of segmenting parasites, we observed a transient outer CP association prior to and during fission in both organelles. Just before the start of segmentation, there is little association between the outer CP and apicoplast. Of 5 parasites imaged that had >10 nuclei but had not yet started segmentation, 3 had no contact points between the outer CP and apicoplast branches and the other 2 had <4 contact points. Once segmentation starts, all apicoplast branches contact an outer CP each and remain in contact with the outer CP until the end of apicoplast fission and centriolar plaque degradation (Figure 6c). In 11 imaged segmenting schizonts, all outer CPs showed contact with an apicoplast branch each. This association starts in early segmentation, when a single branched apicoplast connects all outer CPs. By the time the basal complex reaches maximum diameter and begins contraction, we observe 7 parasites where all branches have completed fission and 2 parasites that had at least one or more apicoplast segments still connecting multiple merozoites (Figure 6c). Mitochondria fission follows a very similar pattern, but later in parasite development. Prior to the basal complex reaching maximum diameter, we observe no significant connection between the outer CP and mitochondria. When the basal complex entered its contraction phase, we observed 9 parasites where all outer CPs were in contact with one branch of the mitochondria each (Figure 5 d&e). Only one of these 9 parasites had an intact pre-fission mitochondrion, while the other 8 had undergone at least one fission event. Matching previous descriptions of mitochondria and apicoplast segmentation, C1-arrested schizonts having completed segmentation show elongated mitochondria (Figure 5a) and small, rounded apicoplasts (Figure 6a).

Both mitochondria and apicoplast fission showed neighbouring nascent merozoites that shared a single branch of mitochondria or apicoplast passing through both of their basal complexes while others had an individual mitochondrion or apicoplast which had already separated from the rest (Figure 5d&6c). This

suggests that fission does not occur synchronously (Figure 5d) and supports the model of branching point fission. In other words, parasites seem to undergo a primary fission event that leaves only some merozoites sharing stretches of the organelles and then a subsequent fission event leaves each merozoite with an individual apicoplast and mitochondrion (Figure 5e). Unfortunately, BODIPY TRc does not distinctly stain the membranes of the mitochondria and apicoplast. So, it is not possible for us to determine whether the observed breaks in staining of our chosen organelle markers truly indicate a complete fission of the mitochondria or apicoplast membranes. Thus, while suggestive of branching point fission, our data is not sufficient to conclusively determine the sequence of fission events in these organelles. More research with additional mitochondrial and apicoplast markers is needed to confirm the observations made in this study and conclusively map out the growth and fission of these organelles.

Characterisation of residual body mitochondria

At the completion of segmentation, the parasite forms a structure known as the residual body, which contains parasite material, such as the hemozoin crystal, that was not incorporated into merozoites during segmentation(Rudlaff et al., 2020). The residual body is poorly understood in *Plasmodium*, but in *Toxoplasma* it has been shown that a significant amount of the mitochondria, and not the apicoplast, is left behind in the residual body following segmentation (Nishi, Hu, Murray, & Roos, 2008).

There is no well-characterized marker of the residual body in *Plasmodium*. So, for this study, we defined the residual body as any area within the parasitophorous vacuole membrane but visibly external to any merozoite in a C1-arrested schizont as determined by BODIPY TRc staining. We imaged 35 C1-arrested schizonts and observed that 54% had mitochondrial staining inside the residual body (Figure 5d and Figure 5 – Figure Supplement 1c). To determine the proportion of total mitochondria that gets included in the residual body, we quantified the fluorescence of both mitochondria in the residual body and mitochondria in merozoites. Of the 19 parasites that showed mitochondria staining inside the residual body, the amount of material ranged from 1% to 12% of the total mitochondrial staining in the parasite (Figure 5 – Figure Supplement 1d). On average, the residual body had approximately 1.5x more mitochondrial staining than the average merozoite (Figure 5 – Figure Supplement 1e). No significant apicoplast staining was ever observed in the residual body, similarly to what has been reported for *Toxoplasma* (Nishi et al., 2008).

Cytostomes

During its intraerythrocytic development, *P. falciparum* engulfs host cell cytoplasm from which it catabolizes haemoglobin as a source of amino acids (Francis, Sullivan, & Goldberg, 1997). The parasite is separated from its host cell by the parasitophorous vacuole, and therefore the uptake of host-cell cytosol requires invagination of both the PPM and PVM. The cytostome coordinates this endocytic process and is comprised of two key regions: a protein-dense collar region, which forms the pore through which membrane invagination will occur, and the membranous bulb region, which contains the RBC-derived cargo (Milani, Schneider, & Taraschi, 2015; Xie, Ralph, & Tilley, 2020).

NHS ester staining reveals pore-like structures at the parasite plasma membrane.

Prior to this study, cytostomes were not immediately obvious by NHS ester staining given the large number of features that were visible using this stain but pending validation. While observing the basal complex of segmenting schizonts (Figure 4a), we noticed that merozoites contained a second NHS-ester-dense ring (Figure 7a). The size and position of this NHS ester ring matched that of an endocytic micropore recently identified in *Toxoplasma* tachyzoites (Koreny et al., 2022). In that study, the micropore was identified using Kelch13 (K13) as a marker (Koreny et al., 2022). The *Plasmodium* equivalent to this K13 micropore is the cytostome, so to determine whether this NHS-ester-dense ring was indeed a cytostome, we evaluated a parasite strain where the endogenous K13 was fused to GFP (Birnbaum et al., 2017). Investigation using this parasite line revealed that the NHS-ester-dense ring also stained with K13, suggesting that this structure is a cytostome (Figure 7b).

PFA-glutaraldehyde fixation allows visualization of cytostome bulb

The cytostome can be divided into two main components: the collar, a protein dense ring at the parasite plasma membrane where K13 is located, and the bulb, a membrane invagination containing red blood cell cytoplasm (Milani et al., 2015; Xie et al., 2020).While we could identify the cytostomal collar by K13 staining, these cytostomal collars were not attached to a membranous invagination. Fixation using 4% v/v paraformaldehyde (PFA) is known to result in the permeabilization of the RBC membrane and loss of its cytoplasmic contents (Tonkin et al., 2004). Topologically, the cytostome is contiguous with the RBC

cytoplasm and so we hypothesised that PFA fixation was resulting in the loss of cytostomal contents and obscuring of the bulb. PFA-glutaraldehyde fixation has been shown to better preserve the RBC cytoplasm (Tonkin et al., 2004). Comparing PFA only with PFA-glutaraldehyde fixed parasites, we could clearly observe that the addition of glutaraldehyde preserves both the RBC membrane and RBC cytoplasmic contents (Figure 7c). Further, while only cytostomal collars could be observed with PFA only fixation, large membrane invaginations (cytostomal bulbs) were observed with PFA-glutaraldehyde fixation (Figure 7d). Cytostomal bulbs were often much longer and more elaborate spreading through much of the parasite (Video 1), but these images are visually complex and difficult to project so images displayed in Figure 7 show relatively smaller cytostomal bulbs. Collectively, this data supports the hypothesis that these NHS-ester-dense rings are indeed cytostomes and that endocytosis can be studied using U-ExM, but PFA-glutaraldehyde fixation is required to maintain cytostome bulb integrity.

We subsequently harvested K13-GFP parasites across the parasite lifecycle and imaged them following either PFA only or PFA-glutaraldehyde fixation. K13-stained cytostomes were detected at all stages of the parasite lifecycle (Figure 7e). Ring-stage parasites typically contained one or two cytostomes, which increased in number during the trophozoite stage and schizogony (Figure 7e).

Single cytostomes appear in the area containing the IMC near the apical organelles at the same time as the basal complex forms a complete ring. Cytostomes remain within the IMC area but change positions within the nascent merozoite as segmentation progresses (Figure 4b, white asterisks). The majority of merozoites in C1-arrested schizonts contained a single cytostome. This suggests that cytostomes are incorporated into the IMC of merozoites and inherited early in segmentation. Clusters of cytostomes that had not been incorporated into merozoites during segmentation were observed either adjacent to nascent merozoites or as part of the residual body (Figure 7 – Figure Supplement 1 and Figure 4b, yellow asterisk). It is currently unclear whether there are any functional differences between the cytostomes that are incorporated into merozoites and those that are left behind.

Non-canonical cytostome collar morphologies

We noticed a number of different cytostome morphologies and organizational patterns (Figure 7 – Figure Supplement 1). Cytostomes frequently clustered together and did not appear randomly distributed

across the PPM (Figure 7e). Some cytostomes would form what appeared to be higher order structures where two or three distinct cytostomal collars appeared to be stacked end-on-end (Figure 7 – Figure Supplement 1). Cytostomes have a relatively well defined and consistent size (Aikawa, 1971; Yang et al., 2019), but occasionally we observed very large cytostomal collars that were approximately twice the diameter of other cytostome collars in the same cell (Figure 7 – Figure Supplement 1). It is unclear what the function of these higher order structures or large cytostomes is, if they represent biogenesis transition states, or indeed if they're performing some specialized endocytosis.

The rhoptries

To invade host red blood cells, merozoites secrete proteins from specialized secretory organelles known as the rhoptries and micronemes. While both the rhoptries and micronemes are well studied in the context of *Plasmodium* biology, neither have been investigated in detail using expansion microscopy in *Plasmodium*. We previously showed that fully formed rhoptries can be observed by NHS ester staining alone (Liffner & Absalon, 2021), but did not investigate their biogenesis.

Rhoptries can be observed from early in their biogenesis using NHS ester staining.

Rhoptries consist of a neck and bulb region, with the tip of the neck being loaded into the apical polar rings of merozoites. Despite both being formed from Golgi-derived cargo, the neck and bulb regions have distinct proteomes (Counihan et al., 2013). We first tracked rhoptry bulb biogenesis across schizogony using antibodies directed against the rhoptry bulb marker rhoptry associated protein 1 (RAP1).

Nascent rhoptries were detected early in schizogony, with RAP1 foci appearing adjacent to all branches of the outer CP from parasites with 6-10 nuclei in a one-to-one ratio, as described above (Figure 8a and Figure 8 -Figure Supplement 1b). These foci co-localized with NHS ester densities of the same size and round shape, no elongated neck-like structures were visible by NHS ester (neck biogenesis described in more detail below). This matches reports that rhoptry bulb biogenesis occurs first (Bannister et al., 2000; Counihan et al., 2013), with neck biogenesis not occurring until segmentation. As early as the last mitotic event during early segmentation, rhoptry bulbs were observed as pairs, with 88 of 93 (95%) centriolar plaques observed forming a mitotic spindle being associated with two RAP1-positive NHS ester densities

per outer CP branch. Finally, in newly invaded ring-stage parasites, strong RAP1 staining was observed at the PPM/PVM (Figure 8 -Figure Supplement 1a), supporting previously reported observations that secreted RAP1 coats the merozoite during invasion (Riglar et al., 2011).

Our data not only suggests that rhoptry biogenesis occurs well before segmentation, when nuclei still have several rounds of mitosis to complete, but also that rhoptries remain centriolar plaque-associated during these mitotic events. Instances of this association with the centriolar plaque have been observed before (Bannister et al., 2000; Rudlaff et al., 2020) but its mechanism remains unknown. To our knowledge, this is the first in-depth documentation of a rhoptry-centriolar plaque association throughout schizogony in *Plasmodium*.

Rhoptry heterogeneity during early schizogony and segmentation.

Rhoptries associated with the same centriolar plaque during early schizogony sometimes differ in size (Figure 8 -Figure Supplement 1b). This is not surprising given the speed of mitotic events requires near-constant biogenesis of new rhoptry bulbs. By the time segmentation is underway, instead of inheriting one sister rhoptry in the final mitotic event of schizogony, each centriolar plaque will inherit a pair of rhoptries each. At this point, the speed of these mitotic events slows and parasites reach a point of semi-synchrony. To our surprise, this synchrony does not extend to rhoptry pairs; the two rhoptries inherited by segmenting daughter cells remain different from each other. This heterogeneity in rhoptry pairs during early segmentation has been documented before by electron microscopy (Bannister et al., 2000; Rudlaff et al., 2020). Of 109 rhoptry pairs imaged in early segmentation schizonts undergoing their last miotic event (where centriolar plaques were observed forming mitotic spindles), only 4% had two rhoptries of similar size and density (Figure 8 -Figure Supplement 1d). We observed that 40% of these 109 rhoptry pairs had different size but equal NHS ester density, 21% had the same size but different NHS ester density, and 35% differed in both size and NHS ester density (Figure 8 -Figure Supplement 1e). As expected from previous reports, this heterogeneity was lost after the completion of this last miotic event and rhoptry neck elongation. Of 98 rhoptry pairs imaged in non-mitotic segmenting parasites, 76% had two rhoptries of similar size and density (Figure 8 -Figure Supplement 1d). It is still unclear how the one-to-two rhoptry transition occurs and whether rhoptry heterogeneity has a biological role in biogenesis and maturation of the organelles.

Overall, we present three main observations suggesting that rhoptry pairs undergo sequential *de novo* biogenesis rather than dividing from a single precursor rhoptry. First, the tight correlation between rhoptry and outer CP branch number suggests that either rhoptry division happens so fast that transition states are not observable with these methods or that each rhoptry forms *de novo* and such transition states do not exist. Second, the heterogeneity in rhoptry size throughout schizogony favors a model of *de novo* biogenesis given that it would be unusual for a single rhoptry to divide into two rhoptries of different sizes. Lastly, well-documented heterogeneity in rhoptry density suggests that, at least during early segmentation, rhoptries have different compositions. Heterogeneity in rhoptry contents would be difficult to achieve so quickly after biogenesis if they formed through fission of a precursor rhoptry. While constant *de novo* biogenesis could explain why one rhoptry can appear smaller or less mature than the other (Bannister et al., 2000; Rudlaff et al., 2020) it is currently unclear why heterogeneity in rhoptry density only appears during early segmentation and not earlier. Thus, this model is not enough to explain all the variation in rhoptry size and density observed throughout schizogony. Furthermore, a lot of unknowns remain about what exactly governs rhoptry number during the rapid rounds of asynchronous nuclear division (Klaus et al., 2022), how the transition to a rhoptry pair is signalled, and how many rounds of *de novo* rhoptry formation parasites undergo.

Rhoptry neck biogenesis and elongation

In order to observe rhoptry neck biogenesis in more detail, we stained parasites against the rhoptry apical membrane antigen (RAMA, a rhoptry bulb marker) and rhoptry neck protein 4 (RON4, a rhoptry neck marker) (Richard et al., 2010; Topolska, Lidgett, Truman, Fujioka, & Coppel, 2004). RAMA is anchored to the rhoptry bulb membrane and only stains the periphery of the rhoptry bulb as marked by NHS ester (Figure 8b and Figure 8 - Figure Supplement 1c). RON4 is absent from the earliest rhoptry bulbs, appearing as a focus within the rhoptry bulb shortly before early segmentation and before the rhoptry neck could be distinguished from the bulb by NHS ester staining alone (Figure 8b). During early segmentation, when rhoptry pairs first become visible, we observe an uneven distribution of RON4 within each pair. RON4 preferentially associates with one of the rhoptries, with the staining on the second rhoptry being fainter, more diffuse, or even absent in some cases. Of 84 rhoptry pairs observed at this stage, 72 (86%) showed an

691 uneven distribution of RON4. To our surprise, when these rhoptry pairs were of different NHS ester
692 densities, the larger share of RON4 associated with the less dense rhoptry (Figure 8b). Previous observations
693 of rhoptry density differences by electron microscopy have been ascribed to differences in rhoptry age or
694 maturity, with the denser rhoptry being more mature. So, finding RON4 to be more abundant in the less
695 dense rhoptry suggests that either heterogenous RON4 accumulation cannot be explained by rhoptry age or
696 that the less dense rhoptry is instead the older rhoptry. The RON4-positive rhoptry neck elongates during
697 segmentation, attaining its characteristic shape by mid to late segmentation and becoming observable by
698 both RON4 staining and NHS ester (Figure 8). At this point, nearly all rhoptry necks had an equal
699 distribution of RON4 (of 76 rhoptry pairs observed at these stages, 72 (95%) had an equal distribution of
700 RON4).

701 **The micronemes**

702 Previous studies have suggested that micronemes may be heterogeneous and that apical membrane
703 antigen 1 (AMA1) and other micronemal markers such as erythrocyte binding antigen-175 (EBA175) reside
704 in different subsets of micronemes (Absalon et al., 2018; Ebrahimzadeh et al., 2019; Healer, Crawford,
705 Ralph, McFadden, & Cowman, 2002). We reasoned that individual micronemes may be visible using U-
706 ExM and imaged parasites stained with AMA1 and EBA175 to observe their biogenesis and relative
707 distribution. The first microneme marker to appear during schizogony was AMA1. Large puncta of AMA1
708 appear near the rhoptries when the basal complex is at its maximum diameter (Figure 9a). At this point,
709 EBA175 is not yet detectable above background fluorescence. At the end of segmentation, we observe
710 AMA1 has arranged itself into small, densely arranged puncta below the APR and around the rhoptry neck.
711 We also observe EBA175 staining in puncta that are less densely arranged and have little co-localization
712 with AMA1. EBA175 puncta are basal to the AMA1 puncta, being closer to the rhoptry bulb. They also
713 form a cloud of larger diameter than the one formed by AMA1 such that, when viewed from above the APR,
714 two concentric clouds are observed with the core being AMA1 positive and the periphery being EBA175
715 positive (Figure 9b&c). We could observe a punctate NHS-ester staining pattern at the apical end of
716 merozoites (Figure 9b), which we reasoned could be micronemes. The AMA1 and EBA175 staining we
717 observed in late-stage schizonts partially overlaps with this punctate NHS-ester pattern, suggesting that

NHS-ester punctae are micronemes (Figure 9c). However, many NHS-ester-positive foci did not stain with either AMA1 or EBA175 despite being morphologically indistinguishable from those which did. This suggests that NHS-ester stains more than just the micronemes and that some of these foci may be exonemes, dense granules, or other apical vesicles. Alternatively, it is also possible that these additional NHS-ester-positive foci represent micronemes that lack both AMA1 and EBA175.

Using the protease inhibitor E64, we arrested parasites "post-egress" such that AMA1 was translocated. E64 allows for normal daughter cell maturation but prevents RBC plasma membrane rupture once segmentation is complete (Hale et al., 2017). We observe that once AMA1 is translocated, the density of apical AMA1 decreases. EBA175, which does not translocate, increases in density, and moves apically, taking the space AMA1 occupied prior to translocation (Figure 9c&d). This is consistent with existing models of sequential microneme translocation and microneme fusion near the APR(Dubois & Soldati-Favre, 2019).

DISCUSSION

In this work, we apply U-ExM to the asexual blood stage of *Plasmodium falciparum* to provide new insights into the role of the centriolar plaque in establishing apical-basal polarity and in coordinating organelle segregation during schizogony. In the process, we demonstrate U-ExM can be used to study the biogenesis and protein distribution of a variety of organelles and structures within the parasite. Globally, our observations suggest that the centriolar plaque is involved in establishing apical-basal polarity within the parasite and that this polarity is established early in schizogony.

We show that the branches of the outer CP appear to act as physical 'tethers', connecting the nucleus to parasite plasma membrane (PPM). This creates a space between the PPM and nuclear envelope where we observe multiple parasite structures and organelles including the Golgi, basal complex, rhoptries, and apical polar rings. These structures and organelles remain centriolar plaque-associated despite the constant movement and segregation of centriolar plaques during mitotic events. In other systems, MTOC or centrosome positioning has been described as a source of cellular polarity, polarizing a cell by directing cargo of secretory organelles to a defined area (Cowan & Hyman, 2004; de Anda et al., 2005; Huse, 2012).

While this has not been previously described in *Plasmodium*, this model fits well with our observation of the Golgi being adjacent to the centriolar plaque throughout schizogony. This Golgi positioning could grant local control over the biogenesis of rhoptries, micronemes, dense granules, and IMC, which are all at least partially formed by Golgi-derived cargo (Counihan et al., 2013; Dubois & Soldati-Favre, 2019; Griffith, Pearce, & Heaslip, 2022; Sloves et al., 2012). While the biogenesis of the apical polar rings seems to also be coupled to the centriolar plaque, we do not yet know how they are nucleated or whether they are also dependent on Golgi-derived cargo.

This study also shows centriolar plaque-coupled organelle segregation and biogenesis to an extent never observed before. Specifically, we observe that the Golgi, rhoptries, and basal complex match the branches of the outer CP in number throughout early schizogony and segregate with centriolar plaques during the mitotic events of schizogony. As this study used fixed cells, we lack the temporal power to precisely define the order of these events. Using known markers of parasite age, however, we describe putative transition states that nascent rhoptries and basal complexes adopt when being segregated with centriolar plaques. We put forward a model where outer CP-associated events occur before inner CP-associated events. That is, the duplication of the outer CP and organelles precedes inner CP duplication and the formation of a mitotic spindle such that this cytoplasmic duplication represents the first identifiable step in the commitment of a nucleus to the next round of mitosis. Interestingly, nuclei can sometimes have centriolar plaques forming a mitotic spindle that have already committed to the next round of mitosis by duplicating their cytoplasmic cargo. That is, a mitotic nucleus can show four outer CP branches and sets of apical organelles at the same time. While this supports our hypothesis that duplication of apical organelles and the outer CP components happens upstream from intra-nuclear mitotic events, it does not tell us how this relates to the genome copy number inside the nucleus. So, we cannot say whether DNA replication and associated checkpoints occur upstream or downstream from the cytoplasmic events that seem to commit a centriolar plaque to mitosis.

Lastly, we contribute important evidence toward hypotheses across several open questions regarding organelle biogenesis and segregation in *Plasmodium*. We observe contacts between the outer CP and both the mitochondria and apicoplast during fission that suggest a role for this structure in monitoring copy

772 number of these organelles. We also document sequential fission events in both the apicoplast and
773 mitochondria that are suggestive of branching point fission. Lastly, we see temporal and spatial localization
774 patterns of AMA1, EBA175, and RON4 that support theories of heterogeneity within the apical organelles.

775 U-ExM represents an affordable and adaptable sample preparation method that can be applied to any
776 microscope to produce images with far greater visible detail than conventional light microscopy platforms.
777 Applying this technique to the visualization of organelle biogenesis and segregation throughout schizogony
778 allowed us to observe these processes in the context of structures that could previously only be investigated
779 in detail using electron microscopy. The flexibility and scalability of this technique allowed us to image
780 more than 600 individual parasites at a variety of developmental stages, increasing the confidence of our
781 observations and giving them some temporal resolution. To our knowledge, this paper represents the most
782 comprehensive study of a single organism using U-ExM, with a total of 13 different subcellular structures
783 investigated.

784 Our inability to pinpoint the nucleation site of the SPMTs or resolve the plasma membrane from the
785 IMC highlights some of the limitations of U-ExM as applied in this work. The subpellicular network that
786 holds IMC1g and lines the cytoplasmic face of the IMC sits approximately 20 nm below the parasite surface,
787 where we would find MSP1(Kudryashev et al., 2012). Thus, the distance between IMC1g and MSP1 post-
788 expansion is around 90nm. This is below our imaging resolution with Airyscan2, and close to the maximum
789 resolution we could achieve through other super-resolution methods compatible with our current setup when
790 antibody effects are considered. Thus, some parasite structures remain beyond the resolution achieved in this
791 study. In order to resolve the IMC from the plasma membrane or resolve multiple apical polar rings using
792 light microscopy, we would need to employ single molecule localization microscopy or iterative expansion
793 microscopy(Louvel et al., 2022), which increases expansion factor to ~20x.

794 We also noticed some drawbacks and artifacts introduced by U-ExM. Most visually striking was that
795 the hemozoin crystal of the food vacuole does not expand (Coronado, Nadovich, & Spadafora, 2014), which
796 leaves a large space that lacks NHS ester staining in the center of the parasite. For nearly all antibodies used
797 in this study, significant off-target fluorescence was observed inside the food vacuole. Thus, U-ExM may
798 not be as useful for studying food vacuole biology. Occasionally, significant SYTOX (DNA stain)

fluorescence was observed at either the nuclear envelope or parasite plasma membrane. It is unclear if this represents an expansion-induced artifact or a PFA-fixation artifact that is only now observable. Lastly, for cells stained with Mitotracker, some non-specific background was observed that seemed to correlate with protein density as observed by NHS-ester.

Malaria parasites have been extensively studied using electron microscopy to determine their ultrastructure and live-cell microscopy to observe their most dynamic processes in real time. Much of what we uncovered in this study involved dynamic processes that are too small to be resolved using conventional live-cell microscopy. Specifically, we made important observations about *P. falciparum* organelle biogenesis and the organization of *Plasmodium* cell division around the centriolar plaque. Rather than a replacement for any existing microscopy techniques, we see U-ExM as a complement to the suite of techniques available to study the cell biology of malaria parasites, which bridges some of the limitations of electron microscopy and live-cell microscopy. As such, there are many parasite processes that are logical candidates for investigation by U-ExM. Some of these have been highlighted in this paper, but others remain completely unexplored. Merozoite invasion, for example, has been well-studied using a variety of microscopy techniques (Geoghegan et al., 2021; Hanssen et al., 2013; Liffner et al., 2022; Riglar et al., 2011; Weiss et al., 2015), but U-ExM would allow us to visualise how all the apical organelles associate with each other and rearrange in three-dimensions across the established time-course (Weiss et al., 2015) of this process. Another logical candidate for investigation by U-ExM is the rapid disassembly of the IMC and other merozoite organelles immediately following invasion(Ferreira et al., 2021), a process where the parasite undergoes rapid and dramatic morphological rearrangements that lie beyond the resolution of live-cell microscopy.

MATERIALS AND METHODS

Plasmodium falciparum **culture**

Unless otherwise stated, all parasites in this study were 3D7-Cas9(Rudlaff et al., 2019). For imaging of the apicoplast, the previously generated ACP-transit-peptide-GFP cell line was used (Florentin et al.,

825 2020). For imaging of Kelch13, the previously generated 2xFKBP-GFP-K13 parasites were used(Birnbaum
826 et al., 2017). For imaging of the basal complex, the previously generated CINCH-smV5 cell line was used
827 (Rudlaff et al., 2019).

828 All parasites were cultured in O^+ human red blood cells at 4% haematocrit in RPMI-1640 containing
829 25 mM HEPES, 50 mg/L hypoxanthine, 0.21% sodium bicarbonate, and 0.5% w/v Albumax II (Trager &
830 Jensen, 1976). All parasite cultures were incubated on a shaker at 37 °C in a gas mixture of 1% O_2, 5% CO_2,
831 and 94% N_2 as previously described. The smHA-tagged Pf3D7_0311800 (ATP Synthase F0 Subunit D) cell
832 line was maintained under selection of 5 nm WR99210. Apicoplast targeting signal-GFP line was
833 maintained under selection of x mm x. 2xFKBP-GFP-K13 parasites were maintained under selection of 0.9
834 µm DSM1.

835 Parasites were routinely synchronised using sorbitol lysis. Briefly, parasite cultures were
836 resuspended in 5% w/v D-sorbitol, resulting in the selective lysis of schizont-stage parasites (Lambros &
837 Vanderberg, 1979).

838 For samples where parasites were arrested as schizonts using either trans-Epoxysuccinyl-L-
839 leucylamido(4guanidino)butane (E64) (Salmon, Oksman, & Goldberg, 2001) or compound 1 (C1) (Helen M.
840 Taylor et al., 2010), late schizont-stage cultures were treated with either 10 µm E64 for ~3h or 5 µm C1 for
841 ~5 hours.

842 **Plasmid generation and transfection**

843 For imaging of the mitochondria, a cell line where ATP-Synthase F0 Subunit D (Pf3D7_0311800) had
844 a C-terminal spaghetti-monster HA tag was generated (Figure 5 – Figure Supplement 2). To create the
845 Pf3D7_0311800 smHA HDR plasmid, the 3D7_0311800 5' and 3' homology regions were PCR amplified
846 from 3D7 genomic DNA with oligonucleotides oJDD4893/oJDD4894 and oJDD4891/oJDD4892,
847 respectively. The two pieces were fused together using Sequence Overlap Extension PCR (SOE PCR) using
848 oJDD4891/oJDD4894 and the piece was digested with NotI/XhoI and ligated with T4 ligase to generate
849 pSAB55. To create the PF3D7_0311800 targeting guide RNA plasmid, oJDD4889/oJDD4890 were

850 annealed, phosphorylated, and ligated into BpiI-digested pRR216 to generate pSAB81. All oligonucleotide
851 sequences are shown in Table 1.

852 For transfection, 100 µg of pSAB55 plasmid was linearized with StuI and transfected into 3D7-Cas9,
853 along with 100 µg of pSAB81. A day following transfection, parasites were treated with 5 nm WR99210
854 until 13 days, when resistant parasites were detected.

855 **Ultrastructure expansion microscopy**

856 Ultrastructure expansion microscopy (U-ExM) was performed as previously described with minor
857 modification (Bertiaux et al., 2021; Gambarotto et al., 2019; Liffner & Absalon, 2021). 12 mm round
858 Coverslips (Fisher Cat. No. NC1129240) were treated with poly-D-lysine for 1 h at 37 °C, washed twice
859 with MilliQ water, and placed in the wells of a 12-well plate. Parasite cultures were set to 0.5% haematocrit,
860 and 1 mL of parasite culture was added to the well containing the coverslip and for 15 min at 37 °C. Culture
861 supernatants were removed, and cultures were fixed with 1 mL of 4% *v*/*v* paraformaldehyde (PFA) in
862 1xPBS for 15 min at 37 °C. For some experiments visualising cytostomes, cultures were instead fixed in 4%
863 v/v PFA + 0.01% v/v glutaraldehyde in 1xPBS. Following fixation, coverslips were washed three times with
864 37 °C PBS before being treated with 1 mL of 1.4 % *v*/*v* formaldehyde/2% *v*/*v* acrylamide (FA/AA) in PBS.
865 Samples were then incubated at 37 °C overnight.

866 Monomer solution (19% *w*/*w* sodium acrylate (Sigma Cat. No. 408220), 10% *v*/*v* acrylamide (Sigma
867 Cat. No. A4058, St. Louis, MO, USA), 0.1% *v*/*v* N,N'-methylenebisacrylamide (Sigma Cat. No. M1533) in
868 PBS) was typically made the night before gelation and stored at −20 °C overnight. Prior to gelation, FA/AA
869 solution was removed from coverslips, and they were washed once in PBS. For gelation, 5 µL of 10% v/v
870 tetraethylenediamine (TEMED; ThermoFisher Cat. No. 17919) and 5 µL of 10% *w*/*v* ammonium persulfate
871 (APS; ThermoFisher Cat. No. 17874) were added to 90 µL of monomer solution and briefly vortexed.
872 Subsequently, 35 µL was pipetted onto parafilm and coverslips were placed (cell side down) on top. Gels
873 were incubated at 37 °C for 30 minutes before being transferred to wells of a 6-well plate containing
874 denaturation buffer (200 mM sodium dodecyl sulphate (SDS), 200 mM NaCl, 50 mM Tris, pH 9). Gels were
875 incubated in denaturation buffer with shaking for 15 minutes, before separated gels were transferred to 1.5

mL tubes containing denaturation buffer. 1.5 mL tubes were incubated at 95 °C for 90 minutes. Following denaturation, gels were transferred to 10 cm Petri dishes containing 25 mL of MilliQ water for the first round of expansion and placed onto a shaker for 30 minutes three times, changing water in between. Gels were subsequently shrunk with two 15-minute washes in 25 mL of 1x PBS, before being transferred to 6-well plates for 30 minutes of blocking in 3% BSA-PBS at room temperature. After blocking, gels were incubated with primary antibodies, diluted in 3%BSA-PBS, overnight. After primary antibody incubation, gels were washed three times in 0.5% v/v PBS-Tween 20 for 10 minutes before incubation with secondary antibodies diluted in 1x PBS for 2.5 hours. Following secondary antibody incubation, gels were again washed three times in PBS-Tween 20, before being transferred back to 10 cm Petri dishes for re-expansion with three 30-minute MilliQ water incubations.

Gels were either imaged immediately following re-expansion, or stored in 0.2% w/v propyl gallate in MilliQ water until imaging. For gels stained with BODIPY TR Ceramide, the fully expanded gel was incubated overnight at room temperature in 0.2% w/v propyl gallate (Acos Organics Cat No. 131581000) solution containing BODIPY TR ceramide (2 μM final concentration).

For parasites stained with Mitotracker Orange CMTMRos (ThermoFisher, M7510), parasite cultures were resuspended in incomplete media (RPMI-1640 containing 25 mM HEPES, 50 mg/L hypoxanthine, and 0.21% sodium bicarbonate) containing 300 nM Mitotracker Orange CMTMRos. Parasites cultures were then stained with Mitotracker for 35 minutes while settling on Poly-D-lysine coated coverslips. From this point, the expansion protocol was followed as described above, with the exception that all steps when possible were carried out protecting the sample from light.

Cryopreservation and thawing of gels.

A proportion of gels imaged in this study were cryopreserved and subsequently thawed prior to imaging (Louvel et al., 2022). Gels were frozen either unstained, following the first round of expansion, or frozen stained, following the second round of expansion. To freeze, a portion of the expanded gel was placed into a 6-well dish and washed three times with 50% glycerol in MilliQ water for 30 minutes. Fresh glycerol was then added, and the gels were stored at -20 °C for future use. To thaw unstained gels, the glycerol was replaced with MilliQ water and incubated at room temperature for 30 minutes. Gels were then

washed and shrunk with three 20-minute washes in 1x PBS at room temperature before proceeding with the antibody staining process normally. Stained gels were thawed with three washes in MilliQ water for 30 minutes before proceeding with imaging as normal.

Stains and antibodies

A comprehensive list of all stains and antibodies used in this study, their working concentrations, and source(s) can be found in Table 2.

Image acquisition

Immediately before imaging, a small slice of gel ~10mm x ~10mm was cut and mounted on an imaging dish (35mm Cellvis coverslip bottomed dishes NC0409658 - FisherScientific) coated with Poly-D lysine. The side of the gel containing sample is placed face down on the coverslip and a few drops of ddH_20 are added after mounting to prevent gel shrinkage due to dehydration during imaging. All images presented in this study were taken using either a Zeiss LSM800 AxioObserver with an Airyscan detector, or a Zeiss LSM900 AxioObserver with an Airyscan 2 detector. Imaging on both microscopes was conducted using a 63x Plan-Apochromat objective lens with a numerical aperture of 1.4. All images were acquired as Z-stacks that had an XY pixel size of 0.035 µm and a Z-slice size of 0.13 µm.

Image analysis

Image processing and presentation

All images were Airyscan processed using 3D processing at moderate filter strength on ZEN Blue Version 3.1 (Zeiss, Oberkochen, Germany).

The majority of images presented in this study are presented as maximum intensity z-projections, but those that contain BODIPY TR Ceramide are presented as average intensity projections for viewing and interpretation purposes.

3D rendering

3D renderings of micronemal proteins AMA1 and EBA175 were produced using the 3D analysis package on ZEN Blue version 3.5.

Measurement of interpolar spindles and subpellicular microtubules

All length measurements reported in this study were obtained using the "Measure 3D distance" function of ZEN Blue Version 3.1. The length of Interpolar spindle microtubules and subpellicular microtubules was determined as the 3D distance between the start and end points of continuously stained stretches of anti-tubulin staining. Interpolar microtubules were defined as those whose staining appeared to contact both centriolar plaques as defined by NHS ester, while non-interpolar microtubules were those that did not meet these criteria. Subpellicular microtubules were only measured in C1-arrested schizonts that had visibly completed segmentation based on the basal complex as visualised by NHS ester. Any microtubule that did not appear connected to the apical polar ring, or extend towards the basal complex, was excluded from the analysis. Cell diameter was defined as the greatest XY distance on any z-slice between two points of the parasite as defined by NHS Ester staining. Merozoite length was defined as the 3D distance between the center of the apical polar rings and basal complex as defined by NHS ester staining.

Apicoplast and mitochondria area analysis

All area measurements presented were obtained using the "Area" function on ZEN Blue Version 3.1. Images were presented as a maximum intensity projection before free hand outlining the apicoplast or the mitochondria in each image. The sum of all fragments was then calculated to find the total area of the organelles per cell.

Mitochondria residual body analysis

In C1-arrested schizonts, the proportion of total mitochondria staining found in the residual body was calculated as follows. Using ZEN Blue version 3.1, a maximum intensity projection of the entire cell was generated and based on the NHS staining, the entire parasite was defined as the region of interest. Signal intensity of the channel staining the mitochondria was calculated inside the full cell, which was defined as total mitochondria fluorescence. Subsequently, the residual body was defined the area within the parasite vacuole, but external to all merozoite plasma membranes, as based on BODIPY TR ceramide staining. A second maximum intensity projection of this subsection of the schizont was made, the residual body was defined as the region of interest and this signal intensity inside this region of interest was defined as residual body mitochondria fluorescence.

To determine residual body mitochondria fluorescence (RB) as % total mitochondria fluorescence (total), the following equation was used:

$$\left(\frac{RB\ fluorescence}{Total\ fluorescence}\right) \times 100$$

In each of the parasites included in this analysis, the number of merozoites was defined as the number of distinct nuclei as determined by SYTOX staining. To determine residual body mitochondria fluorescence as % of one merozoite, the following equation was used:

$$\left(RB\ fluorescence\ \div \left(\frac{Total\ fluorescence - RB\ fluorescence}{Number\ of\ merozoites}\right)\right) \times 100$$

Cells where no mitochondria fluorescence was visible inside the residual body, while visible inside merozoites, were defined as having no residual body mitochondria. An attempt was made to do a similar analysis on apicoplast stained cells, but no visible apicoplast staining was ever observed in the residual body.

Statistical analysis

Estimation of actual distance from expanded samples

Expansion factors for 43 gels used in this study were determined as follows. Gels were assumed to have an initial diameter of 12 mm, as they are formed on a 12 mm diameter coverslip. Gels were subsequently measured following expansion to the nearest whole millimetre, and the expansion factor was defined as the expanded gel diameter divided by the initial gel diameter (12 mm). Gels whose edges were damaged or malformed, and therefore their diameters could not be actually measured, were excluded. Gels in this study had a median expanded diameter of 51 mm, which corresponds to a median expansion factor of 4.25 (Figure 1 – Figure Supplement 1)

Generation of graphs and statistical analysis

All graphs presented in this study were generated using GraphPad PRISM 9. All error bars in this study represent standard deviation. Differences between samples analysed by ANOVA was determined as difference where the p-value was <0.05. For scatterplots, slopes were considered significantly non-zero when the p-value was <0.05.

977 **Data accessibility**

978 Results in this study are underpinned by 647 3D Airyscan images of U-ExM parasites at multiple
979 lifecycle stages with multiple combinations of stains. All images are publicly available through the
980 following data repository: https://doi.org/10.5061/dryad.9s4mw6mp4.

981 AUTHOR CONTRIBUTIONS

982 **Benjamin Liffner:** Conceptualization, Methodology, Formal analysis, Investigation, Data curation, Writing
983 - Original Draft, Writing - Review & Editing, Visualization.

984 **Ana Karla Cepeda Diaz**: Conceptualization, Methodology, Formal analysis, Investigation, Data curation,
985 Writing - Original Draft, Writing -Review & Editing, Visualization, Funding acquisition.

986 **James Blauwkamp**: Formal analysis, Investigation, Data curation, Writing – Original Draft.

987 **David Anaguano**: Investigation, Writing – Review & Editing.

988 **Sonja Frölich:** Methodology.

989 **Vasant Muralidharan**: Resources, Writing – Review & Editing.

990 **Danny W. Wilson**: Writing -Review & Editing.

991 **Jeffrey Dvorin**: Conceptualization, Resources, Writing –Review & Editing, Supervision, Project
992 Administration, Funding Acquisition.

993 **Sabrina Absalon:** Conceptualization, Methodology, Resources, Writing – Review & Editing, Supervision,
994 Project administration, Funding Acquisition.

995

996 ACKNOWLEDGEMENTS

997 We thank David Roos, Akhil Vaidya, and Rodolpho Ornitz Oliveira Souza for insightful discussions,
998 Vincent Louvel for U-ExM expertise and sharing the protocol for cryopreservation and thawing of gels, and
999 Taco Kooij, and Julie Verhoef for their help with MitoTracker experiments and critical reading of the

manuscript. We thank Tobias Spielmann and Isabelle Henshall for generously sharing K13-GFP parasites, and insightful discussion. We thank Julian Rayner, Alan Cowman, Carole Long, BEI Resources (NIAID, NIH), and the European Malaria Reagent Repository for provision of antibodies. This work was supported by NIH R01 AI145941 (JDD) and F31 AI172110 (AKCD), and the American Heart Association 23POST1011626 (BL).

COMPETING INTERESTS

The authors declare no competing interests.

FIGURE LEGENDS

Figure 1: U-ExM workflow and summary of parasite structures imaged in this study.
(a) Diagram of asexual blood stage lifecycle of *P. falciparum*. **(b)** Ultrastructure expansion microscopy (U-ExM) workflow used in this study. PFA = paraformaldehyde, FA = formaldehyde, AA = acrylamide PG = propyl gallate. Snowflake indicates steps where gels were cryopreserved. **(c)** Comparison of brightfield and DAPI staining of unexpanded *P. falciparum* parasites (inset) with *P. falciparum* prepared by U-ExM, stained with NHS Ester (protein density; greyscale) and SYTOX Deep Red (DNA; cyan) and imaged using Airyscan microscopy. Images are maximum-intensity projections, number on image = Z-axis thickness of projection in µm. Scale bars = 2 µm. **(d)** Summary of all organelles, and their corresponding antibodies, imaged by U-ExM in this study.

Figure 2: Centriolar plaque (CP) biogenesis and dynamics.
3D7 parasites were prepared by U-ExM, stained with NHS ester (greyscale), BODIPY TRc (white), SYTOX (cyan) and anti-centrin (outer centriolar plaque (CP); magenta) antibodies and imaged using Airyscan microscopy.. **(a)** Images of whole parasites throughout asexual blood-stage development. **(b)** Whole parasite panel (left) followed by individual centriolar plaque or centriolar plaque pair zooms following our proposed timeline of events in centriolar plaque biogenesis, dynamics, and disassembly. Yellow line = cytoplasmic extensions, blue line = nuclear envelope, green line = parasite plasma membrane. Images are maximum-intensity projections, number on image = Z-axis thickness of projection in µm. White scale bars = 2 µm, yellow scale bars = 500 nm.

Figure 3: Characterisation of intranuclear and subpellicular microtubules.
3D7 parasites were prepared by U-ExM, stained with NHS ester (greyscale), BODIPY TRc (white), SYTOX (cyan) and anti-tubulin (microtubules; magenta) antibodies, and imaged using Airyscan microscopy. **(a)** Images of whole parasites throughout asexual blood-stage development. **(b)** Nuclei in the process of dividing, with their centriolar plaques connected by an interpolar spindle. **(c)** The number and type of microtubule branches in interpolar spindles and **(d)** length of interpolar microtubules. **(e)** Subpellicular microtubules (SPMTs) stained with an anti-poly-glutamylation (PolyE; yellow) antibody. **(f)** Quantification of the number of SPMTs per merozoite from C1-treated schizonts. **(g)** SPMT biogenesis throughout segmentation. **(h)** Model for SPMT biogenesis. PPM = parasite plasma membrane, APRs = apical polar rings, BC = basal complex, CP = centriolar plaque. Images are maximum-intensity projections, number on image = Z-axis thickness of projection in µm. Scale bars = 2 µm.

Figure 4: Basal complex biogenesis and development throughout segmentation.
Parasites expressing an smV5-tagged copy of the basal complex marker CINCH were prepared by U-ExM, stained with NHS ester (greyscale), BODIPY TRc (white), SYTOX (cyan) and anti-V5 (basal complex;

magenta) antibodies and imaged using Airyscan microscopy across segmentation. **(a)** Images of whole parasites throughout asexual blood-stage development. **(b)** Basal complex development during schizogony. The basal complex is formed around the PPM anchor of the outer CP. In nuclei whose outer CP has two branches, and will therefore undergo mitosis, the basal complex rings are duplicated. From early segmentation, the basal complex acquires a stable, expanding ring form. Cytostomes that will form part of merozoites are marked with a white asterisk, while those outside merozoites are marked with a yellow asterisk. Images are maximum-intensity projections, number on image = Z-axis thickness of projection in µm. Scale bars = 2 µm.

Figure 5: Growth and fission of the mitochondrion.

Parasites with an smHA-tagged copy of the ATP Synthase F0 Subunit D (ATPd, Pf3D7_0311800) as a mitochondrial marker were prepared by U-ExM, stained with NHS ester (greyscale), BODIPY TRc (white), SYTOX (cyan) and anti-HA (mitochondrion; magenta) antibodies and imaged using Airyscan microscopy. **(a)** Images of whole parasites throughout asexual blood-stage development. Maximum intensity projections of both a subsection of the cell (partial mito) and the full cell (full mito) are shown. **(b)** ATPd staining was compared against Mitotracker orange CMTMRos (yellow), which showed discontinuous staining in looped regions. **(c)** Area of the mitochondrion was quantified for parasites of varying nucleus number. 73 cells were counted across 4 biological replicates. **** = $p<0.001$, ns = $p>0.05$ by one-way ANOVA, error bars = SD. **(d)** Schizont with mitochondria that have undergone fission (yellow zoom), mitochondria that are shared between two nascent merozoites (black zoom), and mitochondria left outside merozoites in the forming residual body (grey). **(e)** During fission, mitochondria associate with the outer centriolar plaque (oCP). Images are maximum-intensity projections, number on image = Z-axis thickness of projection in µm. White scale bars = 2 µm, yellow scale bars = 500 nm.

Figure 6: Growth and fission of the apicoplast.

Parasites expressing GFP-conjugated to the apicoplast transit signal of ACP ($ACP^{Ts\text{-}GFP}$) were prepared by U-ExM, stained with NHS ester (greyscale), BODIPY TRc (white), SYTOX (cyan) and anti-GFP (apicoplast) (magenta) antibodies and using Airyscan microscopy.**(a)** Images of whole parasites throughout asexual blood-stage development. Maximum intensity projections of both a subsection of the cell (partial mito) and the full cell (full mito) are shown. **(b)** Area of the apicoplast was quantified for parasites of varying nucleus number. 70 cells were counted across 3 biological replicates. **** = $p<0.001$, * = $p<0.05$ by one-way ANOVA, error bars = SD. **(c)** Representative images of the different stages of apicoplast fission. Images are maximum-intensity projections, number on image = Z-axis thickness of projection in µm. Asterisks represent centriolar plaques. Scale bars = 2 µm.

Figure 7: Cytostomes are observable by U-ExM throughout the asexual blood stage of the lifecycle.

(a) Parasites expressing an smV5-tagged copy of the basal complex marker CINCH, prepared by U-ExM, and stained with anti-V5, show NHS ester dense rings that are negative for this basal complex marker. **(b)** Parasites prepared by U-ExM where the cytostome marker Kelch13 was conjugated to GFP (K13-GFP) and stained with anti-GFP. Image shows colocalization between K13-GFP and the putative cytostome. NHS ester-dense ring . **(c)** Comparison between PFA-only and PFA-glutaraldehyde fixed U-ExM parasites, showing lysed (PFA only, orange) and intact (PFA-glutaraldehyde, magenta) RBC membranes. **(d)** In PFA only fixed parasites, only the cytostomal collar is preserved, while both the collar and bulb are preserved upon PFA-glutaraldehyde fixation. **(e)** K13-GFP parasites were either fixed in PFA only or PFA-glutaraldehyde, prepared by U-ExM, stained with NHS ester (greyscale), SYTOX (cyan) and anti-GFP (Cytostome) (magenta) antibodies and imaged using Airyscan microscopy across the asexual blood stage. Zoomed regions show cytostomes\ Images are maximum-intensity projections, number on image = Z-axis thickness of projection in µm. White scale bars = 2 µm. Yellow scale bars = 500 nm.

Figure 8: Rhoptries undergo biogenesis near the centriolar plaque and are segregated during nuclear division.

3D7 parasites were prepared by U-ExM, stained with NHS ester (greyscale), BODIPY TRc (white), SYTOX (cyan) and an anti-rhoptry antibodies and imaged using Airyscan microscopy. **(a)** Images of whole parasites

.093 throughout schizogony stained using an anti-RAP1 (rhoptry bulb; magenta)- antibody. **(b)** Zoom into
.094 rhoptry pairs of 3D7 parasites that were prepared for U-ExM and stained with NHS Ester (greyscale) along
.095 with antibodies against RAMA (rhoptry bulb; magenta) and RON4 (rhoptry neck; yellow) to assess rhoptry
.096 neck biogenesis. We observed that the rhoptry neck begins as a single focus inside each rhoptry. Rhoptries
.097 then get duplicated and segregated alongside the centriolar plaque. During the final mitosis, the rhoptry neck
.098 begins to elongate and the rhoptries separate from centriolar plaque. Images are maximum-intensity
.099 projections, number on image = Z-axis thickness of projection in µm . Scale bars = 2 µm.

.100 **Figure 9: Micronemal proteins AMA1 and EBA175 reside in separate micronemes.**
.101 3D7 parasites were prepared by U-ExM, stained with NHS ester (greyscale), SYTOX (cyan) and antibodies
.102 against the micronemal markers AMA1 (magenta) and EBA-175 (yellow), and imaged using Airyscan
.103 microscopy in segmenting schizonts. **(a)** Images of whole parasites throughout schizogony. In schizonts still
.104 undergoing segmentation, AMA1 localized to the apical end while EBA175 was not detected. In late
.105 schizonts, both EBA175 and AMA1 were present in the micronemes. In E64-arrested schizonts, AMA1 was
.106 translocated to the merozoite surface while EBA175 remained micronemal. 3D rendering **(b)** and zooms **(c)**
.107 of merozoites with either micronemal or translocated AMA1. Foci of AMA1 and EBA175 to not routinely
.108 colocalize with each other. Images are maximum-intensity projections, number on image = Z-axis thickness
.109 of projection in µm. White scale bars = 2 µm, RGB scale bars for 3D rendering = 1 µm.

.110

.111 **Figure 10: Summary of organelle organization and fission during schizogony.**
.112 **(a)** Apical organelle biogenesis: Biogenesis of the rhoptries, Golgi, basal complex, and apical polar rings
.113 occur at outer centriolar plaque (CP), between the nuclear envelope and parasite plasma membrane.
.114 Duplication and segregation of these organelles appears to be tied to centriolar plaque duplication and
.115 segregation following nuclear divison. Mid-segmentation merozoite: The rhoptry neck is distinguishable
.116 from the bulb, and AMA1-positive micronemes are present at the apical end of the forming merozoite. Each
.117 merozoite has inherited a cytostome. Subpellicular microtubules stretch the entire distance from the apical
.118 polar rings and the basal complex. The apicoplast has attached to the outer CP and begun fission. Mature
.119 merozoite: The parasite has completed segmentation, and each merozoite contains a full suite of organelles.
.120 The centriolar plaque is no longer visible, and EBA175-positive micronemes are both visible and separate
.121 from AMA1-positive micronemes. **(b)** Model for fission of the mitochondrion and apicoplast. Prior to
.122 fission, both the apicoplast and mitochondrion branch throughout the parasite cytoplasm, before associating
.123 with the outer CP of each forming merozoite. For the apicoplast, this occurs during the final mitosis, but not
.124 until late in segmentation for the mitochondrion. Following outer CP association, the apicoplast and
.125 mitochondrion undergo a first fission event, which leaves an apicoplast and mitochondrion shared between
.126 forming merozoite pairs. Subsequently both organelles undergo a second fission event, leaving each forming
.127 merozoite with a single apicoplast and mitochondrion.

.128 FIGURE SUPPLEMENT LEGENDS

.129 **Figure 1 – Figure Supplement 1: Size of gels imaged in this study.**

.130 **(a)** 42 of the expanded gels in this study were measured post-expansion to **(b)** calculate their expansion
.131 factor**.** The median gel length was 51 mm, which corresponds to a 4.25x expansion factor, and so for 'actual'
.132 measurements, values were divded by 4.25.

Figure 1 – Figure Supplement 2: Cytoplasm staining during intraerythrocytic development.
3D7 parasites were prepared by U-ExM, stained with NHS Ester (greyscale), BODIPY TRc (white), SYTOX (cyan) and anti-aldolase (cytoplasm; magenta) antibodies and imaged by Airyscan microscopy across the asexual blood-stage. Yellow line indicates likely position of food vacuole lacking hemozoin crystal. Images are maximum-intensity projections, number on image = Z-depth in µm of projection. Scale bars = 2 µm.

Figure 2 – Figure Supplement 1: Characterisation of outer centriolar plaque branches.

(a) Mononucleated 3D7 parasites were prepared by U-ExM, stained with NHS Ester (greyscale), anti-centrin (outer centriolar plaque (CP), magenta) and anti-tubulin (microtubules, yellow) antibodies and imaged by Airyscan microscopy. Nuclei form the first hemispindle before centrin is observed, and associate with the parasite plasma membrane (PPM) following visualisation of centrin. **(b)** Quantification of the number of cytoplasmic extensions (branches) per outer CP in parasites of varying age. Indvidual centriolar plaques from mitotic spindles were assessed separately**. (c)** Quantification of the co-occurrence of outer CP branch number with centrin foci. **(d)** In the 8% of 2 cytoplasmic extension outer CPs that had only a single centrin focus, these were likely non-resolvable at the image resolution. **(e)** Parasites that had started mitosis were stained with NHS Ester and Golgi marker ERD2 (magenta). Golgi was seen associating with centriolar plaques and appeared to duplicate with the formation of the mitotic spindle. Images are maximum-intensity projections, number on image = Z-depth in µm of projection. Scale bars = 2 µm.

Figure 2 – Figure Supplement 2: Golgi staining during intraerythrocytic development.

3D7 parasites were prepared by U-ExM, stained with NHS Ester (greyscale), BODIPY TRc (white), SYTOX (cyan) and anti-ERD2 (Golgi; magenta) antibodies and imaged by Airyscan microscopy across the asexual blood-stage. Images are maximum-intensity projections, number on image = Z-depth in µm of projection. White scale bars = 2 µm, yellow scale bars = 500 nm. 4x Zooms show Golgi-centriolar plaque interaction.

Figure 3 – Figure Supplement 1: Staining of microtubules, centriolar plaque, mitochondrion and apicoplast in rings or early trophozoite stages.

The focus of this study was parasites undergoing schizogony, but multiple ring-stage parasites and mononucleated trophozoites were also imaged. For microtubules and centrin, 3D7 parasites were prepared by U-ExM, stained with NHS Ester (greyscale), BODIPY TRc (white), SYTOX (cyan) and either anti-tubulin (microtubules) or anti-centrin (outer centriolar plaque) (magenta) antibodies and imaged using Airyscan microscopy. For the mitochondrion, ATP synthase F0 subunit D^{smHA} parasites were stained as described for microtubules and centriolar plaque, except with anti-HA (mitochondrion) antibodies. For the apicoplast, parasites expressing a GFP-tagged copy of the apicoplast targeting signal of acyl carrier protein were stained as described previously except with anti-GFP (apicoplast) antibodies. Images are maximum-intensity projections, number on image = Z-depth in µm of projection. Scale bars = 2 µm.

Figure 4 – Figure Supplement 1: Basal complex biogenesis in mitotic nuclei.

(a) Parasites expressing an smV5-tagged copy of the basal complex marker CINCH were prepared by U-ExM, stained with NHS Ester (greyscale), and anti-V5 (basal complex; magenta) antibodies and imaged by Airyscan microscopy across segmentation. All nuclei shown in Figure 4b, which describes basal complex biogenesis, had a single centriolar plaque. This figure shows comparable images of nuclei that have

duplicated their centriolar plaque and have a visible mitotic spindle. **(b)** Maximum intensity projection and 3D rendering during basal complex biogenesis showing semicircles of CINCH staining around the centriolar plaque. Images are maximum-intensity projections, number on image = Z-depth in µm of projection. Scale bars = 2 µm.

Figure 4 – Figure Supplement 2: Endoplasmic reticulum staining during intraerythrocytic development.

3D7 parasites were prepared by U-ExM, stained with NHS Ester (greyscale), BODIPY TRc (white), SYTOX (cyan) and anti-BIP (Endoplasmic reticulum; magenta) antibodies and imaged by Airyscan microscopy across the asexual blood-stage. Images are maximum-intensity projections, number on image = Z-depth in µm of projection. Scale bars = 2 µm.

Figure 4 – Figure Supplement 3: Inner membrane complex progression through segmentation.

(a) 3D7 parasites were prepared by U-ExM, stained with NHS Ester (greyscale), BODIPY TRc (white), SYTOX (cyan) and anti-GAP45 (IMC) (magenta) antibodies and imaged using Airyscan microscopy across segmentation. 3D7 parasites were stained with NHS ester, SYTOX, anti-MSP1 (parasite plasma membrane) and either anti-GAP45 **(b)** or anti-IMC1g **(c)** antibodies. GAP45 resides in the IMC luminal space, while IMC1g resides on the cytosolic side of the IMC. Neither GAP45 or IMC1g could be reliably distinguished from MSP1. Images are maximum-intensity projections, number on image = Z-depth in µm of projection. Scale bars = 2 µm.

Figure 5 – Figure Supplement 1: Comparison of MitoTracker with ATPd staining, and residual body mitochondria quantification.

(a) Parasites with an smHA-tagged copy of the ATP Synthase F0 Subunit D (Pf3D7_0311800), a mitochondrial marker, were prepared by U-ExM, stained with NHS Ester (greyscale), BODIPY TRc (white), SYTOX (cyan), Mitotracker (mitochondrion; yellow) and anti-HA (mitochondrion; magenta) antibodies and imaged Airyscan microscopy across the asexual blood-stage. Maximum intensity projections that showed NHS-Ester, BODIPY and SYTOX of discernible structures often did not give a good indication of mitochondria shape. To address this, projections of both a subsection of the cell (part) and the full cell (full) are shown. **(b)** MitoTracker staining showed numerous punctae along the mitochondrion**. (c)** The percentage of C1-arrested schizonts where mitochondria staining was observed in the residual body (RB) was quantified. This fluorescence was then compared against the total mitochondria fluoresence **(d)** and the mean mitochondria fluorescence of one merozoite within that schizont **(e).** Images are maximum-intensity projections, number on image = Z-depth in µm of projection. Scale bars = 2 µm.

Figure 5 – Figure Supplement 2: Generation of ATPd (Pf3D7_0311800) smHA parasites.

(a) To generate an smHA-tagged copy of ATPd (Pf3D7_0311800), 3D7 Cas9 parasites were transfected with a plasmid that contained a 3' homology region to ATPd, followed by a C-terminal smHA-tag. **(b)** Integration of smHA tag into the ATPd locus was confirmed by PCR.

Figure 7 – Figure Supplement 1: Observed cytostome morphologies.

Parasites expressing a GFP-tagged copy of the cytostome marker Kelch13 (K13-GFP) were prepared for U-ExM, stained with NHS Ester (greyscale) and anti-GFP (cytostome; magenta) antibodies and imaged using

.211 Airyscan microscopy. 'Double' cytostomes where two collars appeared to be stacked on top of each other,
.212 and cytostomes approximately twice the diameter of other cytostomes were occasionally observed.
.213 Additionally, in almost all segmenting schizonts, multiple cytostomes were observed that were not
.214 incorporated into the forming merozoites. Images are maximum-intensity projections, number on image =
.215 Z-depth in µm of projection. Black scale bar = 2 µm, yellow scale bars = 500 nm.

.216 **Figure 8 – Figure Supplement 1: Rhoptry biogenesis during schizogony.**

.217 **(a)** The rhoptry marker RAP1 was observed coating the outside of a recently invaded ring-stage parasite. **(b)**
.218 Different combinations of rhoptries and plaques observed while imaging parasites undergoing schizogony.
.219 **(c)** Representative image of E64-arrested schizont stained with NHS Ester (greyscale), the rhoptry bulb
.220 marker RAMA (magenta) and the rhoptry neck marker RON4 (yellow). **(d)** In early-segmentation schizonts
.221 that were either undergoing their final mitosis, or had completed their final mitosis (post-mitosis), the degree
.222 of hetereogeneity between rhoptry pairs was quantified. Rhoptry pairs that showed visible differences in
.223 either size or NHS ester staining density were considered heterogeneous**. (e)** Breakdown of rhoptries using
.224 different classifications of hereogeneity. Images are maximum-intensity projections, number on image = Z-
.225 depth in µm of projection. Scale bars = 2 µm.

.226 TABLES

Oligo/gBlock Name	Sequence (5'→3')
oJDD44	TGGGGTGATGATAAAATGAAAG
oJDD56	ACACTTTATGCTTCCGGCTCGTATGTTGTG
oJDD4889	TATTGTCAAATCGTTACCTCTATG
oJDD4890	AAACCATAGAGGTAACGATTTGAC
oJDD4891	TAGgcggccgcGGTCCTACACCAATAAATATCA
oJDD4892	GTCTGATTCTTCCCATCaggccttccggaccgcggGGTCCCTTCATTGTAGACTTTTTATTATTGAAC
oJDD4893	GTCTACAATGAAGGGACCccgcggtccggaaggcctGATGGGAAGAATCAGACAAATGGT
oJDD4894	GATctcgagcAGcGGcAAtGAcTTcACgAATTCTCTTATTTCTTGTTTTTGCATTTCCT
oSAB257	CGGACCGAGAATTTATGTCCATTAACGTC
oSAB471	TGGTATTAATGGATGAAGACACACA
oSAB472	GTAATGGAATAGCTTTATATATGTACCTTCAT
oSAB473	TATGTGATCCATACATACCTGTTCAGAC

.227 **Table 1: Oligonucleotides for cloning and integration PCR.**
.228

.229

.230

.231

.232

.233

.234

.235

.236

.237

Primary Antibodies	Ab species	Antibody source (cat. Number)	Ab conc.	Reference
anti-alpha tubulin (Clone B-5-1-2)	Mouse (IgG1)	ThermoFisher (32-2500)	1:500	
anti-centrin (Clone 20H5)	Mouse (IgG2a)	Sigma-Aldrich (04-1624)	1:200	
anti-*Hs*centrin1	Rabbit	ThermoFisher (PA5-29986)	1:500	
anti-polyE (IN105)	Rabbit	Adipogen (AG-25B-0030-C050)	1:500	
anti-ERD2 (MRA-1)	Rabbit	BEI Resources MR4	1:2000	(H.G. Elmendorf & K. Haldar, 1993)
anti-HA (3F10)	Rat	Roche (12158167001)	1:50	
anti-GFP	Rabbit	OriGene (TP401)	1:2000	
anti-RAP1 (2.29)	Mouse	European Malaria Reagent Repository	1:500	(Hall et al., 1983)
anti-RON4	Mouse	Gift from Alan Cowman	1:100	
anti-RAMA	Rabbit	Gift from Ross Coppel	1:200	(Topolska et al., 2004)
anti-AMA1	Rabbit	Gift from Carole Long	1:500	
anti-EBA175 (3D7)	Mouse	Gift from Alan Cowman	1:500	(Sim et al., 2011)
anti-Aldolase	rabbit	Abcam (ab207494)	1:2000	
anti-Histone H3	rabbit	Abcam (ab1791)	1:1000	
anti-BIP	rabbit	Generated by Dvorin Lab	1:2000	
anti-GAP45	Rabbit	Gift from Julian Rayner	1:2000	(Jones, Cottingham, & Rayner, 2009)
anti-IMC1g	Rabbit	Generated by Dvorin Lab	1:1000	(Cepeda Diaz et al., 2023)
anti-MSP1 (1E1)	Rabbit	Gift from Anthony Holder	1:250	(M J Blackman, T J Scott-Finnigan, S Shai, & A A Holder, 1994)
anti-Haemoglobin	Rabbit	ThermoFisher (PA5-102943)	1:1000	

.238

Secondary antibodies	Antibody species	Antibody source	Antibody concentration
anti-mouse IgG Alexa Fluor 488	Goat	ThermoFisher (A28175)	1:500
anti-mouse IgG Alexa Fluor 555	Goat	ThermoFisher (A21428)	1:500
anti-rabbit IgG Alexa Fluor 488	Goat	ThermoFisher (A11034)	1:500
anti-rabbit IgG Alexa fluor 555	Goat	ThermoFisher (A21428)	1:500
anti-rat IgG Alexa fluor 488	Goat	ThermoFisher (A11006)	1:500
anti-mouse IgG2a Alexa fluor 488	Goat	ThermoFisher (A21131)	1:500
anti-mouse IgG1 Alexa fluor 594	Goat	ThermoFisher (A21125)	1:500

.239

Stains	Stain source (Cat. No)	Stain concentration

NHS Ester Alexa fluor 405	ThermoFisher (A30000)	1:250 (8 µM in DMSO
BODIPY TR-Ceramide	ThermoFisher (D7549)	1:500 (2 µM)
SYTOX Deep Red	ThermoFisher (S11381)	1:1000 (1 µM) in DMSO

Table 2: Summary of all antibodies and stains used in this study.

REFERENCES

Absalon, S., Blomqvist, K., Rudlaff, R. M., DeLano, T. J., Pollastri, M. P., & Dvorin, J. D. (2018). Calcium-Dependent Protein Kinase 5 Is Required for Release of Egress-Specific Organelles in *Plasmodium falciparum*. *mBio, 9*(1). doi:10.1128/mBio.00130-18

Aikawa , M. (1967). Ultrastructure of the pellicular complex of *Plasmodium fallax*. *Journal of Cell Biology, 35*(1), 103-113. doi:10.1083/jcb.35.1.103

Aikawa, M. (1971). *Plasmodium:* the fine structure of malarial parasites. *Exp Parasitol, 30*(2), 284-320. doi:10.1016/0014-4894(71)90094-4

Anderson-White, B., Beck, J. R., Chen, C.-T., Meissner, M., Bradley, P. J., & Gubbels, M.-J. (2012). Chapter One - Cytoskeleton Assembly in *Toxoplasma gondii* Cell Division. In K. W. Jeon (Ed.), *International Review of Cell and Molecular Biology* (Vol. 298, pp. 1-31): Academic Press.

Bannister, L. H., Hopkins, J. M., Fowler, R. E., Krishna, S., & Mitchell, G. H. (2000). Ultrastructure of rhoptry development in *Plasmodium falciparum* erythrocytic schizonts. *Parasitology, 121 (Pt 3)*, 273-287. doi:10.1017/s0031182099006320

Barylyuk, K., Koreny, L., Ke, H., Butterworth, S., Crook, O. M., Lassadi, I., . . . Waller, R. F. (2020). A Comprehensive Subcellular Atlas of the *Toxoplasma* Proteome via hyperLOPIT Provides Spatial Context for Protein Functions. *Cell Host & Microbe, 28*(5), 752-766.e759. doi:https://doi.org/10.1016/j.chom.2020.09.011

Ben Chaabene, R., Lentini, G., & Soldati-Favre, D. (2021). Biogenesis and discharge of the rhoptries: Key organelles for entry and hijack of host cells by the Apicomplexa. *Molecular Microbiology, 115*(3), 453-465. doi:https://doi.org/10.1111/mmi.14674

Bertiaux, E., Balestra, A. C., Bournonville, L., Louvel, V., Maco, B., Soldati-Favre, D., . . . Hamel, V. (2021). Expansion microscopy provides new insights into the cytoskeleton of malaria parasites including the conservation of a conoid. *PLoS Biol, 19*(3), e3001020. doi:10.1371/journal.pbio.3001020

Birnbaum, J., Flemming, S., Reichard, N., Soares, A. B., Mesén-Ramírez, P., Jonscher, E., . . . Spielmann, T. (2017). A genetic system to study *Plasmodium falciparum* protein function. *Nature Methods, 14*(4), 450-456. doi:10.1038/nmeth.4223

Blackman, M. J., Scott-Finnigan, T. J., Shai, S., & Holder, A. A. (1994). Antibodies inhibit the protease-mediated processing of a malaria merozoite surface protein. *Journal of Experimental Medicine, 180*(1), 389-393. doi:10.1084/jem.180.1.389

Blackman, M. J., Scott-Finnigan, T. J., Shai, S., & Holder, A. A. (1994). Antibodies inhibit the protease-mediated processing of a malaria merozoite surface protein. *J Exp Med, 180*(1), 389-393. doi:10.1084/jem.180.1.389

Collins, C. R., Hackett, F., Strath, M., Penzo, M., Withers-Martinez, C., Baker, D. A., & Blackman, M. J. (2013). Malaria parasite cGMP-dependent protein kinase regulates blood stage merozoite secretory organelle discharge and egress. *PLoS Pathog, 9*(5), e1003344. doi:10.1371/journal.ppat.1003344

Coronado, L. M., Nadovich, C. T., & Spadafora, C. (2014). Malarial hemozoin: from target to tool. *Biochim Biophys Acta, 1840*(6), 2032-2041. doi:10.1016/j.bbagen.2014.02.009

Counihan, N. A., Kalanon, M., Coppel, R. L., & de Koning-Ward, T. F. (2013). *Plasmodium* rhoptry proteins: why order is important. *Trends in Parasitology, 29*(5), 228-236. doi:10.1016/j.pt.2013.03.003

Cowan, C. R., & Hyman, A. A. (2004). Centrosomes direct cell polarity independently of microtubule assembly in *C. elegans* embryos. *Nature, 431*(7004), 92-96. doi:10.1038/nature02825

Dave, N., LaFavers, K., & Arrizabalaga, G. (2022). The Dually Localized EF-Hand Domain-Containing Protein TgEFP1 Regulates the Lytic Cycle of *Toxoplasma gondii*. *Cells, 11*(10). doi:10.3390/cells11101709

de Anda, F. C., Pollarolo, G., Da Silva, J. S., Camoletto, P. G., Feiguin, F., & Dotti, C. G. (2005). Centrosome localization determines neuronal polarity. *Nature, 436*(7051), 704-708. doi:10.1038/nature03811

Cepeda Diaz, A. K., Rudlaff, R. M., Farringer, M., & Dvorin, J. D. (2023). Essential function of alveolin *Pf*IMC1g in the *Plasmodium falciparum* asexual blood stage. *mBio,* e01507-01523. doi:doi:10.1128/mbio.01507-23

Dubois, D. J., & Soldati-Favre, D. (2019). Biogenesis and secretion of micronemes in *Toxoplasma gondii*. *Cellular Microbiology, 21*(5), e13018. doi:https://doi.org/10.1111/cmi.13018

Ebrahimzadeh, Z., Mukherjee, A., Crochetière, M.-È., Sergerie, A., Amiar, S., Thompson, L. A., . . . Richard, D. (2019). A pan-apicomplexan phosphoinositide-binding protein acts in malarial microneme exocytosis. *EMBO reports, 20*(6), e47102. doi:https://doi.org/10.15252/embr.201847102

Elmendorf, H. G., & Haldar, K. (1993). Identification and localization of ERD2 in the malaria parasite *Plasmodium falciparum*: separation from sites of sphingomyelin synthesis and implications for organization of the Golgi. *Embo j, 12*(12), 4763-4773. doi:10.1002/j.1460-2075.1993.tb06165.x

Elmendorf, H. G., & Haldar, K. (1993). Identification and localization of ERD2 in the malaria parasite *Plasmodium falciparum*: separation from sites of sphingomyelin synthesis and implications for organization of the Golgi. *The EMBO Journal, 12*(12), 4763-4773. doi:https://doi.org/10.1002/j.1460-2075.1993.tb06165.x

Elmore, S. P., Nishimura, Y., Qian, T., Herman, B., & Lemasters, J. J. (2004). Discrimination of depolarized from polarized mitochondria by confocal fluorescence resonance energy transfer. *Arch Biochem Biophys, 422*(2), 145-152. doi:10.1016/j.abb.2003.12.031

Engelberg, K., Bechtel, T., Michaud, C., Weerapana, E., & Gubbels, M.-J. (2022). Proteomic characterization of the *Toxoplasma gondii* cytokinesis machinery portrays an expanded hierarchy of its assembly and function. *Nature Communications, 13*(1), 4644. doi:10.1038/s41467-022-32151-0

Esveld, S. L. v., Meerstein-Kessel, L., Boshoven, C., Baaij, J. F., Barylyuk, K., Coolen, J. P. M., . . . Huynen, M. A. (2021). A Prioritized and Validated Resource of Mitochondrial Proteins in *Plasmodium* Identifies Unique Biology. *mSphere, 6*(5), e00614-00621. doi:doi:10.1128/mSphere.00614-21

Evers, F., Cabrera-Orefice, A., Elurbe, D. M., Kea-te Lindert, M., Boltryk, S. D., Voss, T. S., . . . Kooij, T. W. A. (2021). Composition and stage dynamics of mitochondrial complexes in *Plasmodium falciparum*. *Nature Communications, 12*(1), 3820. doi:10.1038/s41467-021-23919-x

Evers, F., Roverts, R., Boshoven, C., Kea-te Lindert, M., Sinden, R. E., Akiva, A., & Kooij, T. W. A. (2023). Comparative 3D ultrastructure of *Plasmodium falciparum* gametocytes. *bioRxiv*, 2023.2003.2010.531920. doi:10.1101/2023.03.10.531920

Ferreira, J. L., Heincke, D., Wichers, J. S., Liffner, B., Wilson, D. W., & Gilberger, T.-W. (2021). The Dynamic Roles of the Inner Membrane Complex in the Multiple Stages of the Malaria Parasite. *Frontiers in Cellular and Infection Microbiology, 10*. doi:10.3389/fcimb.2020.611801

Florentin, A., Stephens, D. R., Brooks, C. F., Baptista, R. P., & Muralidharan, V. (2020). Plastid biogenesis in malaria parasites requires the interactions and catalytic activity of the Clp proteolytic system. *Proceedings of the National Academy of Sciences, 117*(24), 13719-13729. doi:doi:10.1073/pnas.1919501117

Francia, M. E., & Striepen, B. (2014). Cell division in apicomplexan parasites. *Nature Reviews Microbiology, 12*(2), 125-136. doi:10.1038/nrmicro3184

Francis, S. E., Sullivan, D. J., Jr., & Goldberg, D. E. (1997). Hemoglobin metabolism in the malaria parasite *Plasmodium falciparum*. *Annu Rev Microbiol, 51*, 97-123. doi:10.1146/annurev.micro.51.1.97

Gambarotto, D., Zwettler, F. U., Le Guennec, M., Schmidt-Cernohorska, M., Fortun, D., Borgers, S., . . . Guichard, P. (2019). Imaging cellular ultrastructures using expansion microscopy (U-ExM). *Nature Methods, 16*(1), 71-74. doi:10.1038/s41592-018-0238-1

Geoghegan, N. D., Evelyn, C., Whitehead, L. W., Pasternak, M., McDonald, P., Triglia, T., . . . Rogers, K. L. (2021). 4D analysis of malaria parasite invasion offers insights into erythrocyte membrane

remodeling and parasitophorous vacuole formation. *Nature Communications, 12*(1), 3620. doi:10.1038/s41467-021-23626-7

Gerald, N., Mahajan, B., & Kumar, S. (2011). Mitosis in the human malaria parasite *Plasmodium falciparum*. *Eukaryot Cell, 10*(4), 474-482. doi:10.1128/ec.00314-10

Griffith, M. B., Pearce, C. S., & Heaslip, A. T. (2022). Dense granule biogenesis, secretion, and function in *Toxoplasma gondii*. *J Eukaryot Microbiol, 69*(6), e12904. doi:10.1111/jeu.12904

Grüring, C., Heiber, A., Kruse, F., Ungefehr, J., Gilberger, T. W., & Spielmann, T. (2011). Development and host cell modifications of *Plasmodium falciparum* blood stages in four dimensions. *Nat Commun, 2*, 165. doi:10.1038/ncomms1169

Gurnett, A. M., Liberator, P. A., Dulski, P. M., Salowe, S. P., Donald, R. G., Anderson, J. W., . . . Schmatz, D. M. (2002). Purification and molecular characterization of cGMP-dependent protein kinase from Apicomplexan parasites. A novel chemotherapeutic target. *J Biol Chem, 277*(18), 15913-15922. doi:10.1074/jbc.M108393200

Hale, V. L., Watermeyer, J. M., Hackett, F., Vizcay-Barrena, G., van Ooij, C., Thomas, J. A., . . . Saibil, H. R. (2017). Parasitophorous vacuole poration precedes its rupture and rapid host erythrocyte cytoskeleton collapse in *Plasmodium falciparum* egress. *Proceedings of the National Academy of Sciences, 114*(13), 3439-3444. doi:doi:10.1073/pnas.1619441114

Hall, R., McBride, J., Morgan, G., Tait, A., Zolg, J. W., Walliker, D., & Scaife, J. (1983). Antigens of the erythrocytes stages of the human malaria parasite *Plasmodium falciparum* detected by monoclonal antibodies. *Mol Biochem Parasitol, 7*(3), 247-265. doi:10.1016/0166-6851(83)90025-7

Hanssen, E., Dekiwadia, C., Riglar, D. T., Rug, M., Lemgruber, L., Cowman, A. F., . . . Ralph, S. A. (2013). Electron tomography of *Plasmodium falciparum* merozoites reveals core cellular events that underpin erythrocyte invasion. *Cellular Microbiology, 15*(9), 1457-1472. doi:https://doi.org/10.1111/cmi.12132

Harding, C. R., & Meissner, M. (2014). The inner membrane complex through development of *Toxoplasma gondii* and *Plasmodium*. *Cellular Microbiology, 16*(5), 632-641. doi:https://doi.org/10.1111/cmi.12285

Healer, J., Crawford, S., Ralph, S., McFadden, G., & Cowman, A. F. (2002). Independent Translocation of Two Micronemal Proteins in Developing *Plasmodium falciparum* Merozoites. *Infection and Immunity, 70*(10), 5751-5758. doi:doi:10.1128/IAI.70.10.5751-5758.2002

Hu, G., Cabrera, A., Kono, M., Mok, S., Chaal, B. K., Haase, S., . . . Bozdech, Z. (2010). Transcriptional profiling of growth perturbations of the human malaria parasite *Plasmodium falciparum*. *Nature Biotechnology, 28*(1), 91-98. doi:10.1038/nbt.1597

Hu, K. (2008). Organizational Changes of the Daughter Basal Complex during the Parasite Replication of *Toxoplasma gondii*. *PLOS Pathogens, 4*(1), e10. doi:10.1371/journal.ppat.0040010

Huse, M. (2012). Microtubule-organizing center polarity and the immunological synapse: protein kinase C and beyond. *Frontiers in Immunology, 3*. doi:10.3389/fimmu.2012.00235

Jones, M. L., Cottingham, C., & Rayner, J. C. (2009). Effects of calcium signaling on *Plasmodium falciparum* erythrocyte invasion and post-translational modification of gliding-associated protein 45 (PfGAP45). *Molecular and Biochemical Parasitology, 168*(1), 55-62. doi:https://doi.org/10.1016/j.molbiopara.2009.06.007

Jones, M. L., Kitson, E. L., & Rayner, J. C. (2006). *Plasmodium falciparum* erythrocyte invasion: A conserved myosin associated complex. *Molecular and Biochemical Parasitology, 147*(1), 74-84. doi:https://doi.org/10.1016/j.molbiopara.2006.01.009

Kinnunen, M., Kauppila, A., Karmenyan, A., & Myllylä, R. (2011). Effect of the size and shape of a red blood cell on elastic light scattering properties at the single-cell level. *Biomed Opt Express, 2*(7), 1803-1814. doi:10.1364/boe.2.001803

Klaus, S., Binder, P., Kim, J., Machado, M., Funaya, C., Schaaf, V., . . . Ganter, M. (2022). Asynchronous nuclear cycles in multinucleated *Plasmodium falciparum* facilitate rapid proliferation. *Science Advances, 8*(13), eabj5362. doi:doi:10.1126/sciadv.abj5362

Kono, M., Herrmann, S., Loughran, N. B., Cabrera, A., Engelberg, K., Lehmann, C., . . . Gilberger, T. W. (2012). Evolution and Architecture of the Inner Membrane Complex in Asexual and Sexual Stages of the Malaria Parasite. *Molecular Biology and Evolution, 29*(9), 2113-2132. doi:10.1093/molbev/mss081

Koreny, L., Mercado-Saavedra, B. N., Klinger, C. M., Barylyuk, K., Butterworth, S., Hirst, J., . . . Waller, R. F. (2022). Stable and ancient endocytic structures navigate the complex pellicle of apicomplexan parasites. *bioRxiv*, 2022.2006.2002.494549. doi:10.1101/2022.06.02.494549

Kudryashev, M., Münter, S., Lemgruber, L., Montagna, G., Stahlberg, H., Matuschewski, K., . . . Frischknecht, F. (2012). Structural basis for chirality and directional motility of *Plasmodium* sporozoites. *Cell Microbiol, 14*(11), 1757-1768. doi:10.1111/j.1462-5822.2012.01836.x

Kumar, N., Koski, G., Harada, M., Aikawa, M., & Zheng, H. (1991). Induction and localization of *Plasmodium falciparum* stress proteins related to the heat shock protein 70 family. *Molecular and Biochemical Parasitology, 48*(1), 47-58. doi:https://doi.org/10.1016/0166-6851(91)90163-Z

Lambros, C., & Vanderberg, J. P. (1979). Synchronization of *Plasmodium falciparum* erythrocytic stages in culture. *J Parasitol, 65*(3), 418-420.

Li, J., Shami, G. J., Cho, E., Liu, B., Hanssen, E., Dixon, M. W. A., & Tilley, L. (2022). Repurposing the mitotic machinery to drive cellular elongation and chromatin reorganisation in *Plasmodium falciparum* gametocytes. *Nature Communications, 13*(1), 5054. doi:10.1038/s41467-022-32579-4

Liffner, B., & Absalon, S. (2021). Expansion Microscopy Reveals *Plasmodium falciparum* Blood-Stage Parasites Undergo Anaphase with A Chromatin Bridge in the Absence of Mini-Chromosome Maintenance Complex Binding Protein. *Microorganisms, 9*(11), 2306. Retrieved from https://www.mdpi.com/2076-2607/9/11/2306

Liffner, B., & Absalon, S. (2022). Hand-in-hand advances in microscopy and *Plasmodium* nuclear biology. *Trends in Parasitology, 38*(6), 421-423. doi:https://doi.org/10.1016/j.pt.2022.03.007

Liffner, B., Balbin, J. M., Shami, G. J., Siddiqui, G., Strauss, J., Frölich, S., . . . Wilson, D. W. (2022). Cell biological analysis reveals an essential role for *Pfcerli2* in erythrocyte invasion by malaria parasites. *Communications Biology, 5*(1), 121. doi:10.1038/s42003-022-03020-9

Louvel, V., Haase, R., Mercey, O., Laporte, M. H., Soldati-Favre, D., Hamel, V., & Guichard, P. (2022). Nanoscopy of organelles and tissues with iterative ultrastructure expansion microscopy (iU-ExM). *bioRxiv*, 2022.2011.2014.516383. doi:10.1101/2022.11.14.516383

Machado, M., Klaus, S., Klaschka, D., Guizetti, J., & Ganter, M. (2022). *Plasmodium falciparum* CRK4 links early mitotic events to the onset of S-phase during schizogony. *bioRxiv*, 2022.2008.2031.505163. doi:10.1101/2022.08.31.505163

Mahajan, B., Selvapandiyan, A., Gerald, N. J., Majam, V., Zheng, H., Wickramarachchi, T., . . . Kumar, S. (2008). Centrins, Cell Cycle Regulation Proteins in Human Malaria Parasite *Plasmodium falciparum*. *Journal of Biological Chemistry, 283*(46), 31871-31883. doi:https://doi.org/10.1074/jbc.M800028200

Marks, D. L., Bittman, R., & Pagano, R. E. (2008). Use of Bodipy-labeled sphingolipid and cholesterol analogs to examine membrane microdomains in cells. *Histochem Cell Biol, 130*(5), 819-832. doi:10.1007/s00418-008-0509-5

Milani, K. J., Schneider, T. G., & Taraschi, T. F. (2015). Defining the morphology and mechanism of the hemoglobin transport pathway in *Plasmodium falciparum*-infected erythrocytes. *Eukaryot Cell, 14*(4), 415-426. doi:10.1128/ec.00267-14

Morano, A. A., & Dvorin, J. D. (2021). The Ringleaders: Understanding the Apicomplexan Basal Complex Through Comparison to Established Contractile Ring Systems. *Frontiers in Cellular and Infection Microbiology, 11*. doi:10.3389/fcimb.2021.656976

Morrissette, N. S., & Sibley, L. D. (2002). Cytoskeleton of Apicomplexan Parasites. *Microbiology and Molecular Biology Reviews, 66*(1), 21-38. doi:doi:10.1128/MMBR.66.1.21-38.2002

Nanda, J. S., & Lorsch, J. R. (2014). Labeling a protein with fluorophores using NHS ester derivitization. *Methods Enzymol, 536*, 87-94. doi:10.1016/b978-0-12-420070-8.00008-8

Nishi, M., Hu, K., Murray, J. M., & Roos, D. S. (2008). Organellar dynamics during the cell cycle of *Toxoplasma gondii*. *Journal of Cell Science, 121*(9), 1559-1568. doi:10.1242/jcs.021089

Oliveira Souza, R. O., Jacobs, K. N., Back, P. S., Bradley, P. J., & Arrizabalaga, G. (2022). IMC10 and LMF1 mediate mitochondrial morphology through mitochondrion-pellicle contact sites in *Toxoplasma gondii*. *J Cell Sci, 135*(22). doi:10.1242/jcs.260083

Poot, M., Zhang, Y. Z., Krämer, J. A., Wells, K. S., Jones, L. J., Hanzel, D. K., . . . Haugland, R. P. (1996). Analysis of mitochondrial morphology and function with novel fixable fluorescent stains. *J Histochem Cytochem, 44*(12), 1363-1372. doi:10.1177/44.12.8985128

Qian, P., Wang, X., Guan, C., Fang, X., Cai, M., Zhong, C.-q., . . . Yuan, J. (2022). Apical anchorage and stabilization of subpellicular microtubules by apical polar ring ensures *Plasmodium* ookinete infection in mosquito. *Nature Communications, 13*(1), 7465. doi:10.1038/s41467-022-35270-w

Rashpa, R., & Brochet, M. (2022). Expansion microscopy of *Plasmodium* gametocytes reveals the molecular architecture of a bipartite microtubule organisation centre coordinating mitosis with axoneme assembly. *PLoS Pathog, 18*(1), e1010223. doi:10.1371/journal.ppat.1010223

Rashpa, R., Klages, N., Schvartz, D., Pasquarello, C., & Brochet, M. (2023). The Skp1-Cullin1-FBXO1 complex is a pleiotropic regulator required for the formation of gametes and motile forms in *Plasmodium berghei*. *Nature Communications, 14*(1), 1312. doi:10.1038/s41467-023-36999-8

Richard, D., MacRaild, C. A., Riglar, D. T., Chan, J.-A., Foley, M., Baum, J., . . . Cowman, A. F. (2010). Interaction between *Plasmodium falciparum* Apical Membrane Antigen 1 and the Rhoptry Neck Protein Complex Defines a Key Step in the Erythrocyte Invasion Process of Malaria Parasites. *Journal of Biological Chemistry, 285*(19), 14815-14822. doi:https://doi.org/10.1074/jbc.M109.080770

Riglar, D. T., Richard, D., Wilson, D. W., Boyle, M. J., Dekiwadia, C., Turnbull, L., . . . Baum, J. (2011). Super-Resolution Dissection of Coordinated Events during Malaria Parasite Invasion of the Human Erythrocyte. *Cell Host & Microbe, 9*(1), 9-20. doi:10.1016/j.chom.2010.12.003

Roumégous, C., Abou Hammoud, A., Fuster, D., Dupuy, J.-W., Blancard, C., Salin, B., . . . Frénal, K. (2022). Identification of new components of the basal pole of *Toxoplasma gondii* provides novel insights into its molecular organization and functions. *Frontiers in Cellular and Infection Microbiology, 12*. doi:10.3389/fcimb.2022.1010038

Rudlaff, R. M., Kraemer, S., Marshman, J., & Dvorin, J. D. (2020). Three-dimensional ultrastructure of *Plasmodium falciparum* throughout cytokinesis. *PLOS Pathogens, 16*(6), e1008587. doi:10.1371/journal.ppat.1008587

Rudlaff, R. M., Kraemer, S., Streva, V. A., & Dvorin, J. D. (2019). An essential contractile ring protein controls cell division in *Plasmodium falciparum*. *Nature Communications, 10*(1), 2181. doi:10.1038/s41467-019-10214-z

Salmon, B. L., Oksman, A., & Goldberg, D. E. (2001). Malaria parasite exit from the host erythrocyte: a two-step process requiring extraerythrocytic proteolysis. *Proceedings of the National Academy of Sciences, 98*(1), 271-276.

Sanchez, A. D., & Feldman, J. L. (2017). Microtubule-organizing centers: from the centrosome to non-centrosomal sites. *Curr Opin Cell Biol, 44*, 93-101. doi:10.1016/j.ceb.2016.09.003

Severo, V., Souza, R., Vitorino, F., Cunha, J., Ávila, A., Arrizabalaga, G., & Nardelli, S. (2022). Previously Unidentified Histone H1-Like Protein Is Involved in Cell Division and Ribosome Biosynthesis in *Toxoplasma gondii*. *mSphere, 7*(6), e0040322. doi:10.1128/msphere.00403-22

Sheiner, L., Demerly, J. L., Poulsen, N., Beatty, W. L., Lucas, O., Behnke, M. S., . . . Striepen, B. (2011). A Systematic Screen to Discover and Analyze Apicoplast Proteins Identifies a Conserved and Essential Protein Import Factor. *PLOS Pathogens, 7*(12), e1002392. doi:10.1371/journal.ppat.1002392

Sim, B. K. L., Narum, D. L., Chattopadhyay, R., Ahumada, A., Haynes, J. D., Fuhrmann, S. R., . . . Hoffman, S. L. (2011). Delineation of Stage Specific Expression of *Plasmodium falciparum* EBA-175 by Biologically Functional Region II Monoclonal Antibodies. *PLOS ONE, 6*(4), e18393. doi:10.1371/journal.pone.0018393

Simon, C. S., Funaya, C., Bauer, J., Voβ, Y., Machado, M., Penning, A., . . . Guizetti, J. (2021). An extended DNA-free intranuclear compartment organizes centrosome microtubules in malaria parasites. *Life Science Alliance, 4*(11), e202101199. doi:10.26508/lsa.202101199

Sloves, P.-J., Delhaye, S., Mouveaux, T., Werkmeister, E., Slomianny, C., Hovasse, A., . . . Tomavo, S. (2012). *Toxoplasma* Sortilin-like Receptor Regulates Protein Transport and Is Essential for Apical Secretory Organelle Biogenesis and Host Infection. *Cell Host & Microbe, 11*(5), 515-527. doi:10.1016/j.chom.2012.03.006

Taylor, H. M., McRobert, L., Grainger, M., Sicard, A., Dluzewski, A. R., Hopp, C. S., . . . Baker, D. A. (2010). The malaria parasite cyclic GMP-dependent protein kinase plays a central role in blood-stage schizogony. *Eukaryot Cell, 9*(1), 37-45. doi:10.1128/ec.00186-09

Taylor, H. M., McRobert, L., Grainger, M., Sicard, A., Dluzewski, A. R., Hopp, C. S., . . . Baker, D. A. (2010). The Malaria Parasite Cyclic GMP-Dependent Protein Kinase Plays a Central Role in Blood-Stage Schizogony. *Eukaryotic Cell, 9*(1), 37-45. doi:doi:10.1128/EC.00186-09

Tomasina, R., Gonzalez, F. C., Martins-Duarte, É. S., Bastin, P., Gissot, M., & Francia, M. E. (2022). Separate To Operate: the Centriole-Free Inner Core of the Centrosome Regulates the Assembly of the Intranuclear Spindle in *Toxoplasma gondii*. *mBio, 13*(5), e01859-01822. doi:doi:10.1128/mbio.01859-22

Tonkin, C. J., van Dooren, G. G., Spurck, T. P., Struck, N. S., Good, R. T., Handman, E., . . . McFadden, G. I. (2004). Localization of organellar proteins in *Plasmodium falciparum* using a novel set of transfection vectors and a new immunofluorescence fixation method. *Molecular and Biochemical Parasitology, 137*(1), 13-21. doi:https://doi.org/10.1016/j.molbiopara.2004.05.009

Topolska, A. E., Lidgett, A., Truman, D., Fujioka, H., & Coppel, R. L. (2004). Characterization of a membrane-associated rhoptry protein of *Plasmodium falciparum*. *J Biol Chem, 279*(6), 4648-4656. doi:10.1074/jbc.M307859200

Tosetti, N., Dos Santos Pacheco, N., Bertiaux, E., Maco, B., Bournonville, L., Hamel, V., . . . Soldati-Favre, D. (2020). Essential function of the alveolin network in the subpellicular microtubules and conoid assembly in *Toxoplasma gondii*. *eLife, 9*, e56635. doi:10.7554/eLife.56635

Trager, W., & Jensen, J. B. (1976). Human malaria parasites in continuous culture. *Science, 193*(4254), 673-675. doi:10.1126/science.781840

Tran, J. Q., de Leon, J. C., Li, C., Huynh, M. H., Beatty, W., & Morrissette, N. S. (2010). RNG1 is a late marker of the apical polar ring in *Toxoplasma gondii*. *Cytoskeleton (Hoboken), 67*(9), 586-598. doi:10.1002/cm.20469

van Dooren, G. G., Marti, M., Tonkin, C. J., Stimmler, L. M., Cowman, A. F., & McFadden, G. I. (2005). Development of the endoplasmic reticulum, mitochondrion and apicoplast during the asexual life cycle of *Plasmodium falciparum*. *Molecular Microbiology, 57*(2), 405-419. doi:https://doi.org/10.1111/j.1365-2958.2005.04699.x

van Dooren, G. G., Stimmler, L. M., & McFadden, G. I. (2006). Metabolic maps and functions of the *Plasmodium* mitochondrion. *FEMS Microbiology Reviews, 30*(4), 596-630. doi:10.1111/j.1574-6976.2006.00027.x

Verhoef, J. M. J., Meissner, M., & Kooij, T. W. A. (2021). Organelle Dynamics in Apicomplexan Parasites. *mBio, 12*(4), e0140921. doi:10.1128/mBio.01409-21

Viswanathan, S., Williams, M. E., Bloss, E. B., Stasevich, T. J., Speer, C. M., Nern, A., . . . Looger, L. L. (2015). High-performance probes for light and electron microscopy. *Nature Methods, 12*(6), 568-576. doi:10.1038/nmeth.3365

Voß, Y., Klaus, S., Ganter, M., & Guizetti, J. (2022). Ca^{2+}-inducible phase separation of centrins in proliferating malaria parasites. *bioRxiv*, 2022.2007.2026.501452. doi:10.1101/2022.07.26.501452

Wassie, A. T., Zhao, Y., & Boyden, E. S. (2019). Expansion microscopy: principles and uses in biological research. *Nature Methods, 16*(1), 33-41. doi:10.1038/s41592-018-0219-4

Weiss, G. E., Gilson, P. R., Taechalertpaisarn, T., Tham, W.-H., de Jong, N. W. M., Harvey, K. L., . . . Crabb, B. S. (2015). Revealing the Sequence and Resulting Cellular Morphology of Receptor-Ligand Interactions during *Plasmodium falciparum* Invasion of Erythrocytes. *PLOS Pathogens, 11*(2), e1004670. doi:10.1371/journal.ppat.1004670

Wolf, D. M., Segawa, M., Kondadi, A. K., Anand, R., Bailey, S. T., Reichert, A. S., . . . Shirihai, O. S. (2019). Individual cristae within the same mitochondrion display different membrane potentials and are functionally independent. *The EMBO Journal, 38*(22), e101056. doi:https://doi.org/10.15252/embj.2018101056

Xie, S. C., Ralph, S. A., & Tilley, L. (2020). K13, the Cytostome, and Artemisinin Resistance. *Trends in Parasitology, 36*(6), 533-544. doi:10.1016/j.pt.2020.03.006

Yang, T., Yeoh, L. M., Tutor, M. V., Dixon, M. W., McMillan, P. J., Xie, S. C., . . . Cobbold, S. A. (2019). Decreased K13 Abundance Reduces Hemoglobin Catabolism and Proteotoxic Stress, Underpinning Artemisinin Resistance. *Cell Reports, 29*(9), 2917-2928.e2915. doi:https://doi.org/10.1016/j.celrep.2019.10.095

a

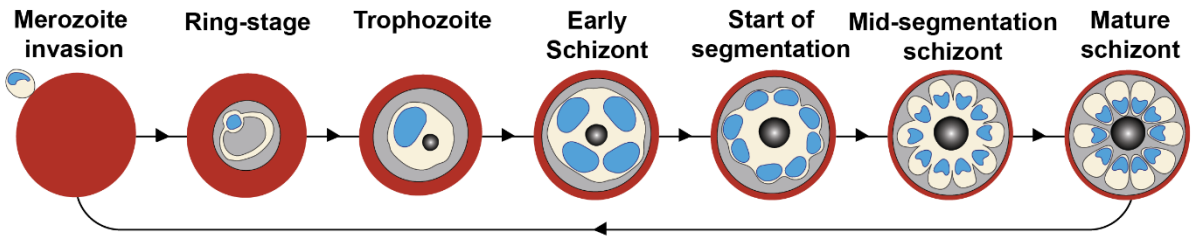

b

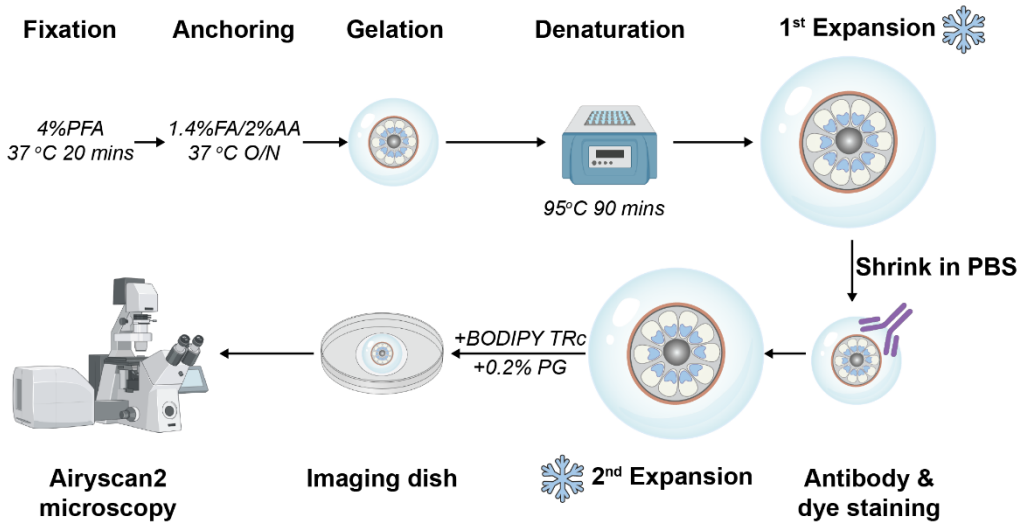

c

U-ExM *Plasmodium falciparum* (unexpanded inset)

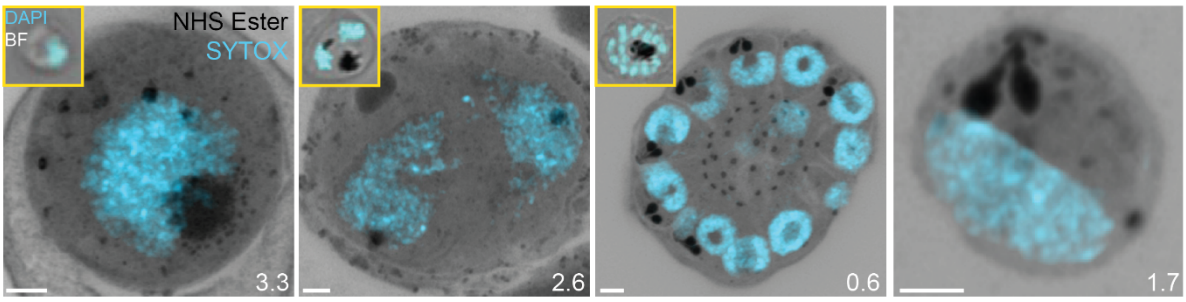

d

Organelles (and markers) imaged in this study			
Centriolar plaque (Centrin)	Microtubules (Tubulin)	Basal Complex (CINCH)	Mitochondrion (ATPd/MitoTracker)
Apicoplast ($ACP^{TS\text{-}GFP}$)	Cytostomes ($K13^{GFP}$)	Rhoptry neck (RON4)	Rhoptry bulb (RAP1/RAMA)
Micronemes (AMA1/EBA175)	Cytoplasm (Aldolase)	Endoplasmic reticulum (BIP)	Golgi (ERD2)
Inner membrane complex (GAP45/IMC1g)			

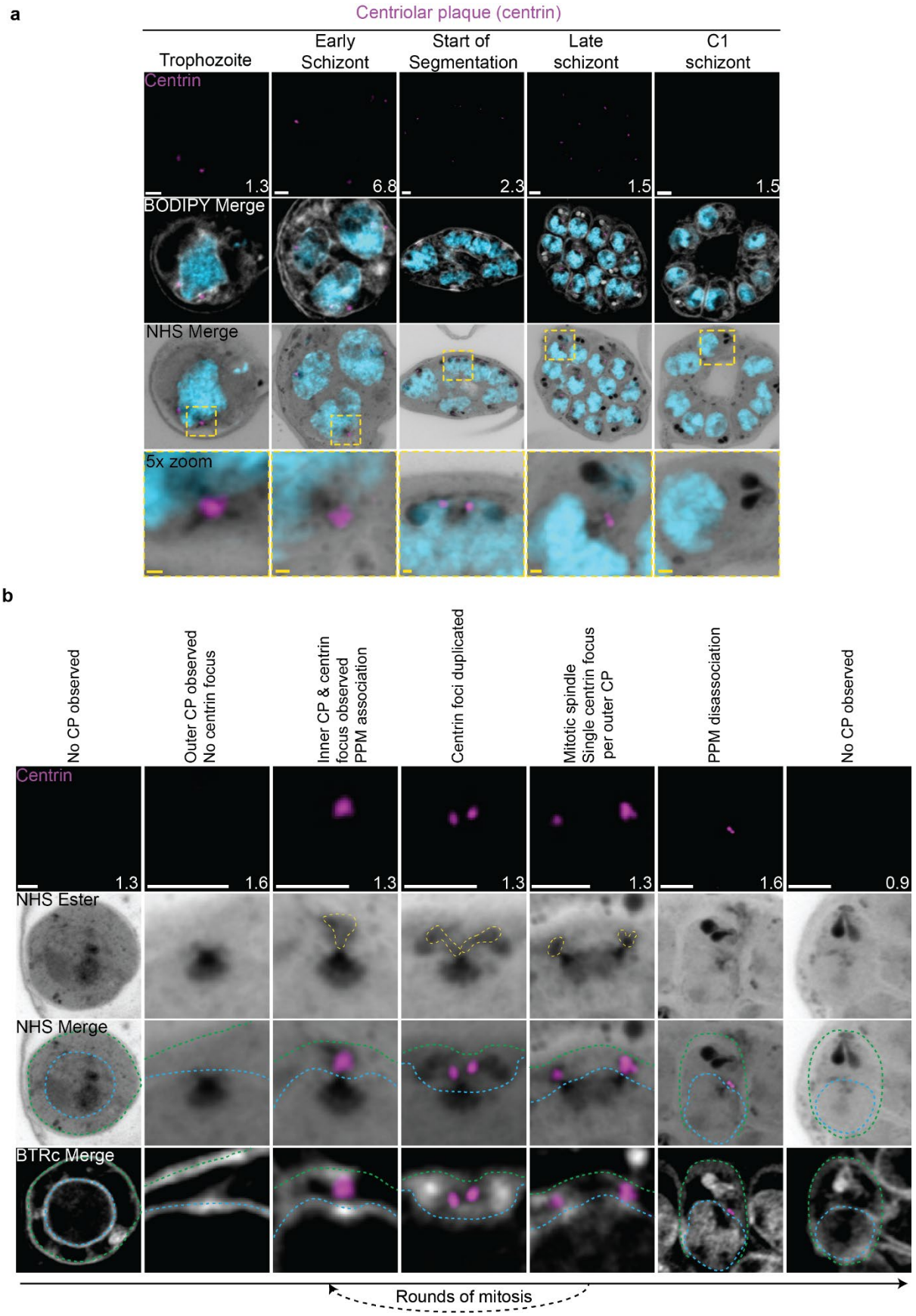
a
Centriolar plaque (centrin)
Trophozoite
Early Schizont
Start of Segmentation
Late schizont
C1 schizont
Centrin
1.3
6.8
2.3
1.5
1.5
BODIPY Merge
NHS Merge
5x zoom
b
No CP observed
Outer CP observed No centrin focus
Inner CP & centrin focus observed PPM association
Centrin foci duplicated
Mitotic spindle Single centrin focus per outer CP
PPM disassociation
No CP observed
Centrin
1.3
1.6
1.3
1.3
1.3
1.6
0.9
NHS Ester
NHS Merge
BTRc Merge
Rounds of mitosis

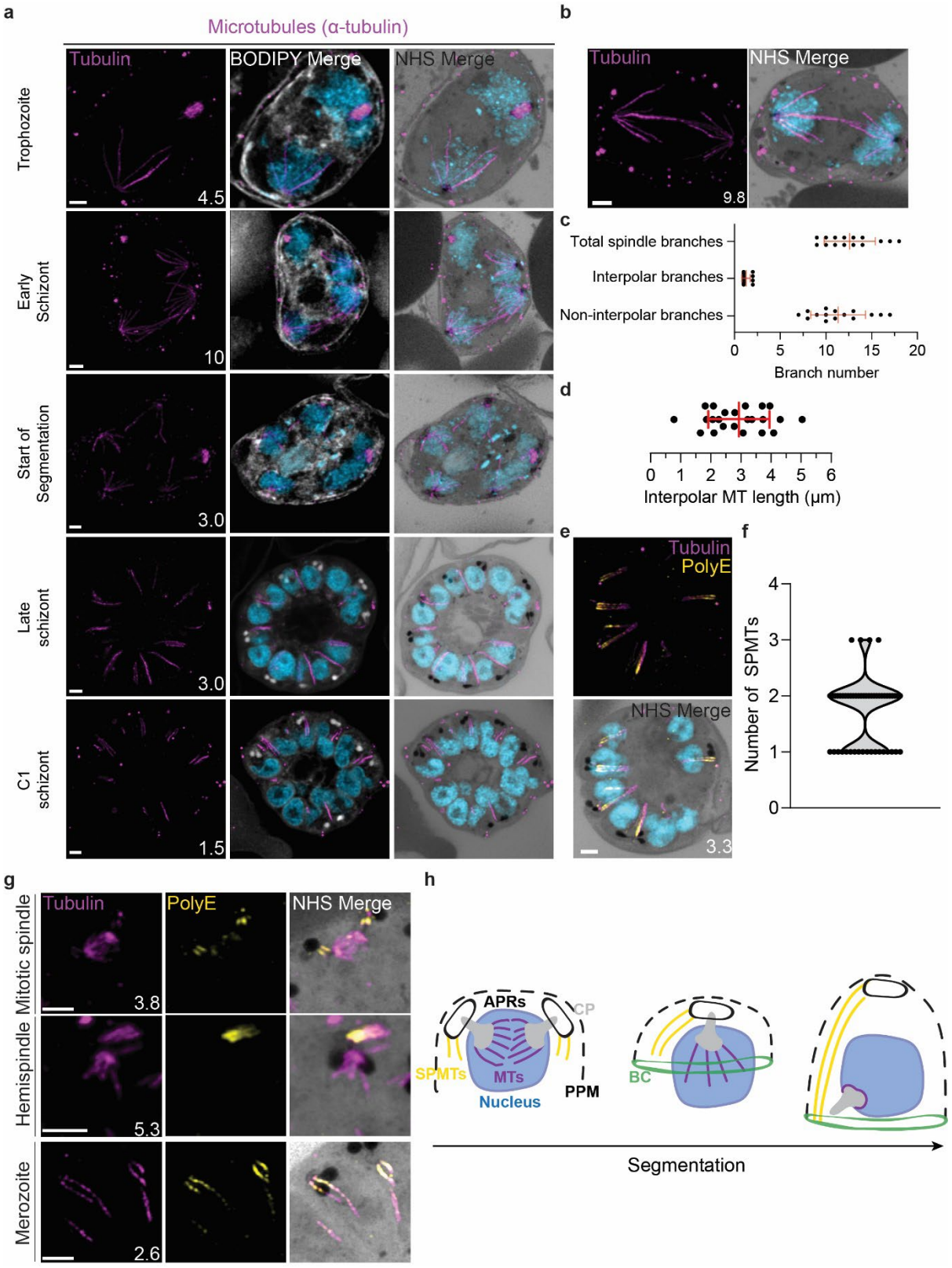
a
Microtubules (α-tubulin)
Tubulin
BODIPY Merge
NHS Merge
Trophozoite
Early Schizont
Start of Segmentation
Late schizont
C1 schizont
4.5
10
3.0
3.0
1.5
b
Tubulin
NHS Merge
9.8
c
Total spindle branches
Interpolar branches
Non-interpolar branches
0
5
10
15
20
Branch number
d
0
1
2
3
4
5
6
Interpolar MT length (μm)
e
Tubulin
PolyE
NHS Merge
3.3
f
Number of SPMTs
0
1
2
3
4
g
Tubulin
PolyE
NHS Merge
Mitotic spindle
Hemispindle
Merozoite
3.8
5.3
2.6
h
APRs
CP
SPMTs
MTs
Nucleus
PPM
BC
Segmentation

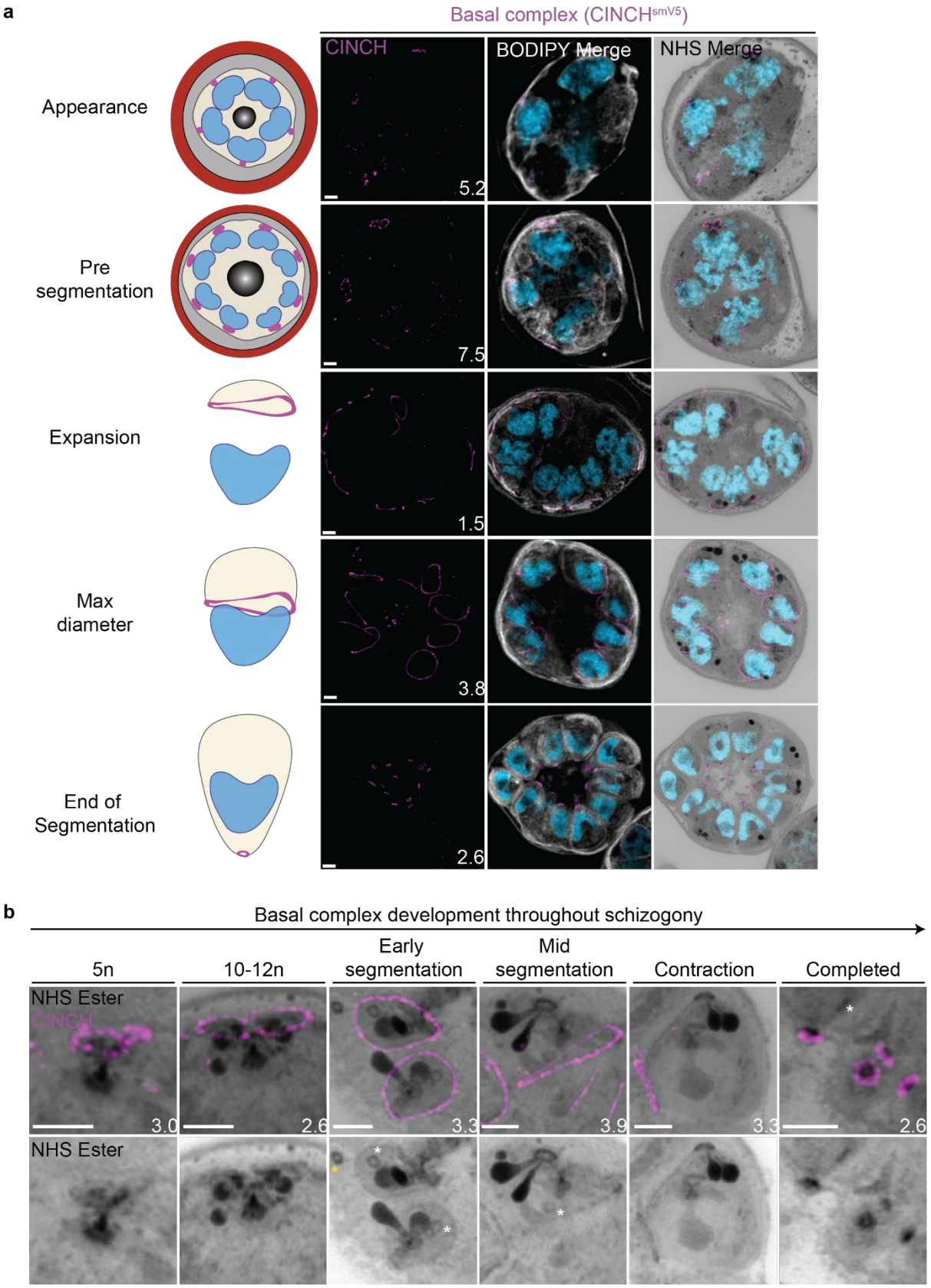
a
Basal complex (CINCHsmV5)
CINCH
BODIPY Merge
NHS Merge
Appearance
Pre segmentation
Expansion
Max diameter
End of Segmentation
5.2
7.5
1.5
3.8
2.6
b
Basal complex development throughout schizogony
5n
10-12n
Early segmentation
Mid segmentation
Contraction
Completed
NHS Ester
CINCH
3.0
2.6
3.3
3.9
3.3
2.6
NHS Ester

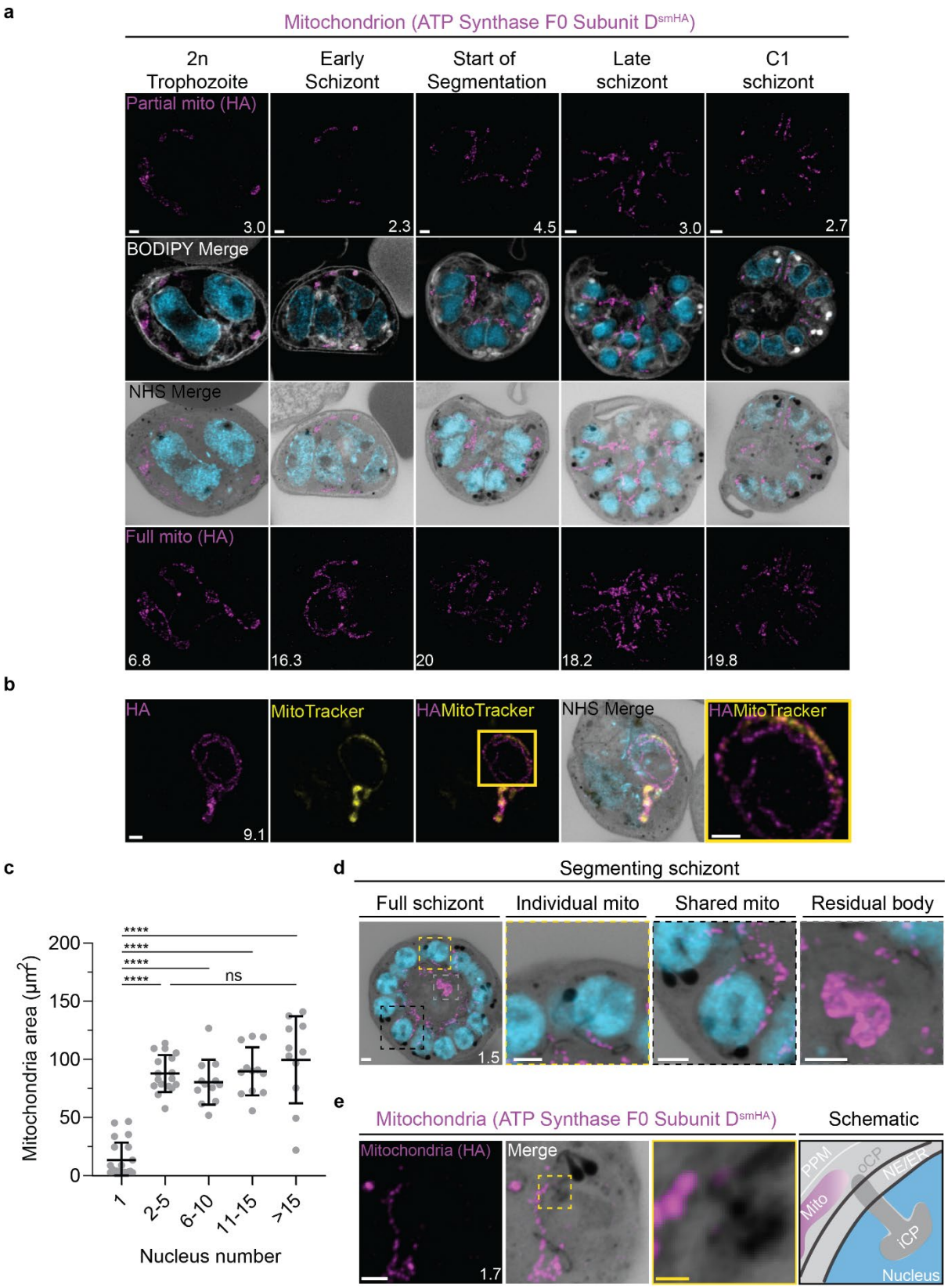
a
Mitochondrion (ATP Synthase F0 Subunit D^{smHA})
2n Trophozoite
Early Schizont
Start of Segmentation
Late schizont
C1 schizont
Partial mito (HA)
3.0
2.3
4.5
3.0
2.7
BODIPY Merge
NHS Merge
Full mito (HA)
6.8
16.3
20
18.2
19.8
b
HA
MitoTracker
HAMitoTracker
NHS Merge
HAMitoTracker
9.1
c
Mitochondria area (µm²)
200
150
100
50
0
****
****
****
****
ns
1
2-5
6-10
11-15
>15
Nucleus number
d
Segmenting schizont
Full schizont
Individual mito
Shared mito
Residual body
1.5
e
Mitochondria (ATP Synthase F0 Subunit D^{smHA})
Schematic
Mitochondria (HA)
Merge
1.7
PPM
oCP
NE/ER
Mito
iCP
Nucleus

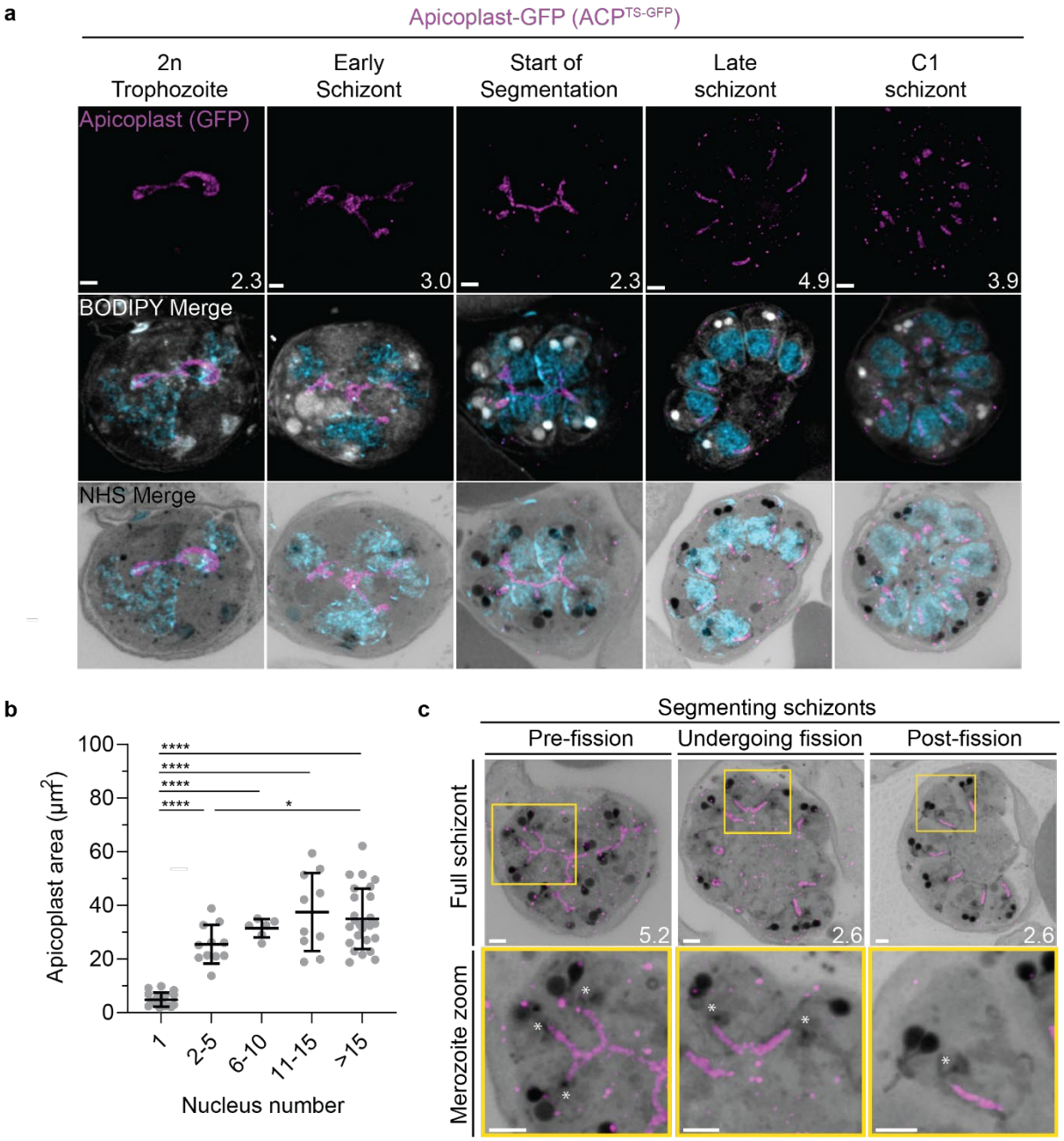
a
Apicoplast-GFP (ACP^TS-GFP)
2n Trophozoite
Early Schizont
Start of Segmentation
Late schizont
C1 schizont
Apicoplast (GFP)
2.3
3.0
2.3
4.9
3.9
BODIPY Merge
NHS Merge
b
Apicoplast area (µm²)
100
80
60
40
20
0
****
****
****
****
*
1
2-5
6-10
11-15
>15
Nucleus number
c
Segmenting schizonts
Pre-fission
Undergoing fission
Post-fission
Full schizont
Merozoite zoom
5.2
2.6
2.6

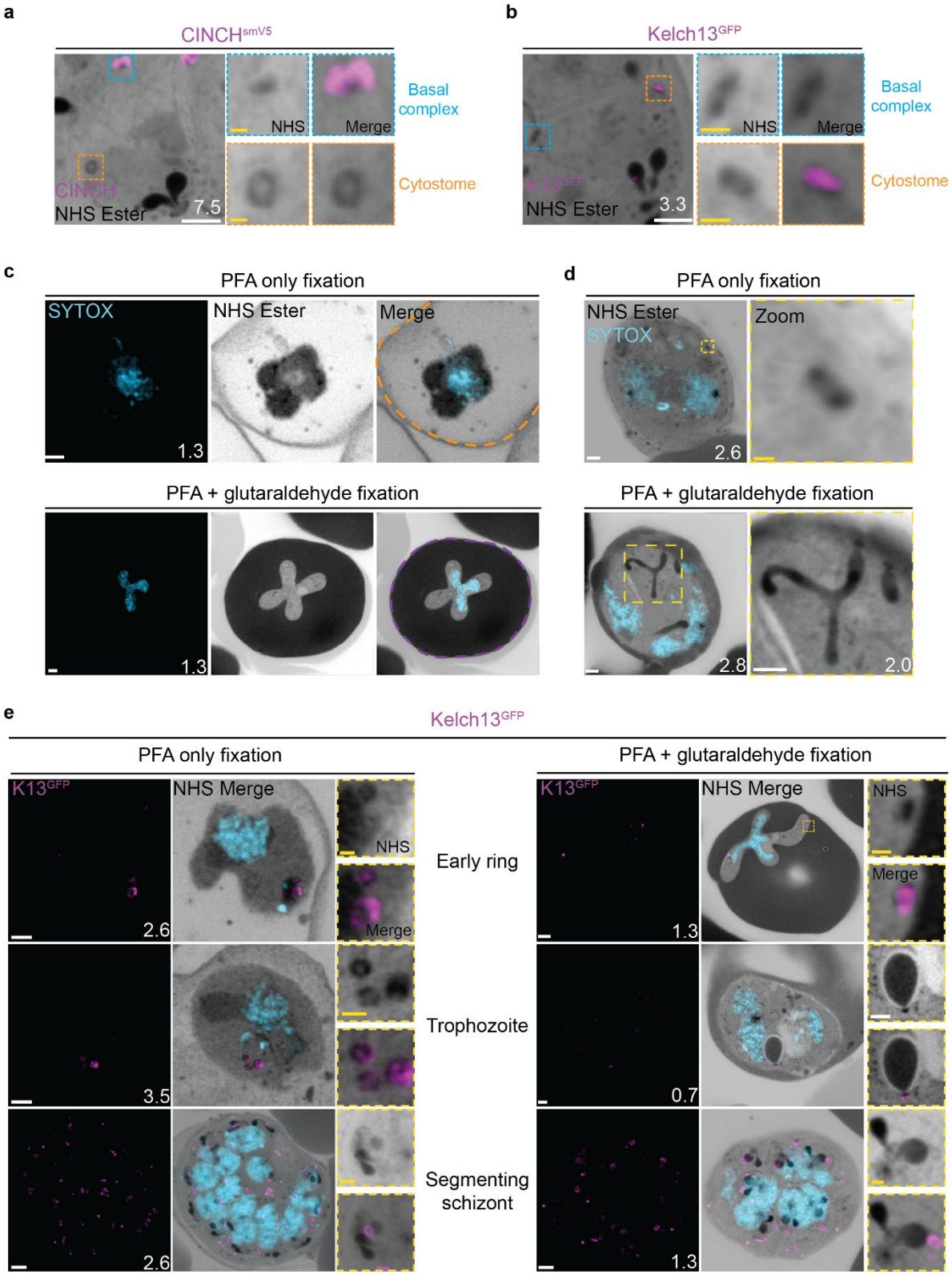
a
CINCHsmV5
Basal complex
Cytostome
NHS
Merge
CINCH
NHS Ester
7.5
b
Kelch13GFP
Basal complex
Cytostome
NHS
Merge
K13GFP
NHS Ester
3.3
c
PFA only fixation
SYTOX
NHS Ester
Merge
1.3
PFA + glutaraldehyde fixation
1.3
d
PFA only fixation
NHS Ester
SYTOX
Zoom
2.6
PFA + glutaraldehyde fixation
2.8
2.0
e
Kelch13GFP
PFA only fixation
PFA + glutaraldehyde fixation
K13GFP
NHS Merge
NHS
Merge
Early ring
Trophozoite
Segmenting schizont
2.6
3.5
2.6
1.3
0.7
1.3

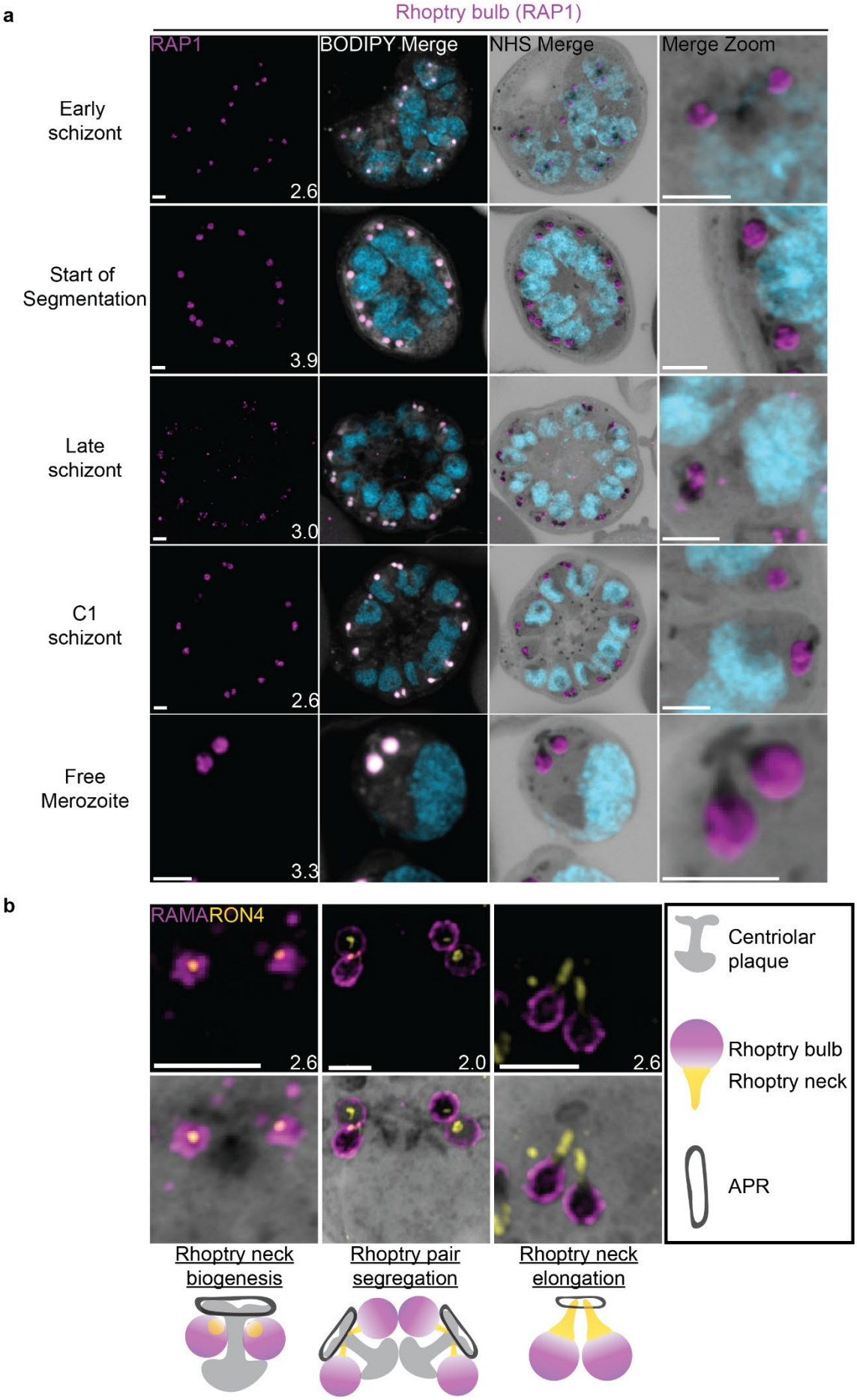
a
Rhoptry bulb (RAP1)
RAP1
BODIPY Merge
NHS Merge
Merge Zoom
Early schizont
Start of Segmentation
Late schizont
C1 schizont
Free Merozoite
2.6
3.9
3.0
2.6
3.3
b
RAMARON4
2.6
2.0
2.6
Centriolar plaque
Rhoptry bulb
Rhoptry neck
APR
Rhoptry neck biogenesis
Rhoptry pair segregation
Rhoptry neck elongation

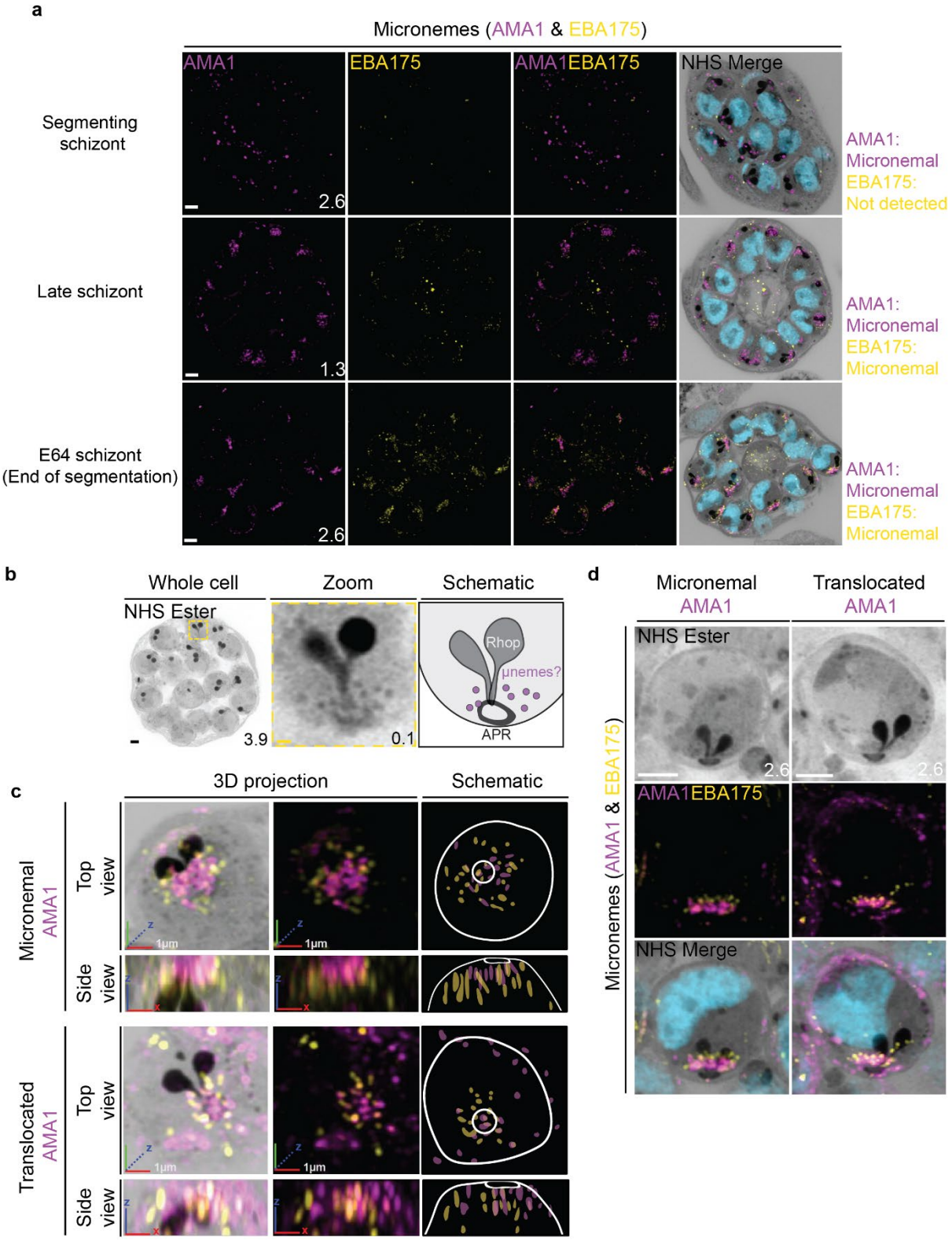
a
Micronemes (AMA1 & EBA175)
AMA1
EBA175
AMA1EBA175
NHS Merge
Segmenting schizont
Late schizont
E64 schizont (End of segmentation)
2.6
1.3
2.6
AMA1: Micronemal
EBA175: Not detected
AMA1: Micronemal
EBA175: Micronemal
AMA1: Micronemal
EBA175: Micronemal
b
Whole cell
Zoom
Schematic
NHS Ester
3.9
0.1
Rhop
μnemes?
APR
c
3D projection
Schematic
Micronemal AMA1
Translocated AMA1
Top view
Side view
1μm
d
Micronemal AMA1
Translocated AMA1
NHS Ester
AMA1EBA175
NHS Merge
Micronemes (AMA1 & EBA175)
2.6
2.6

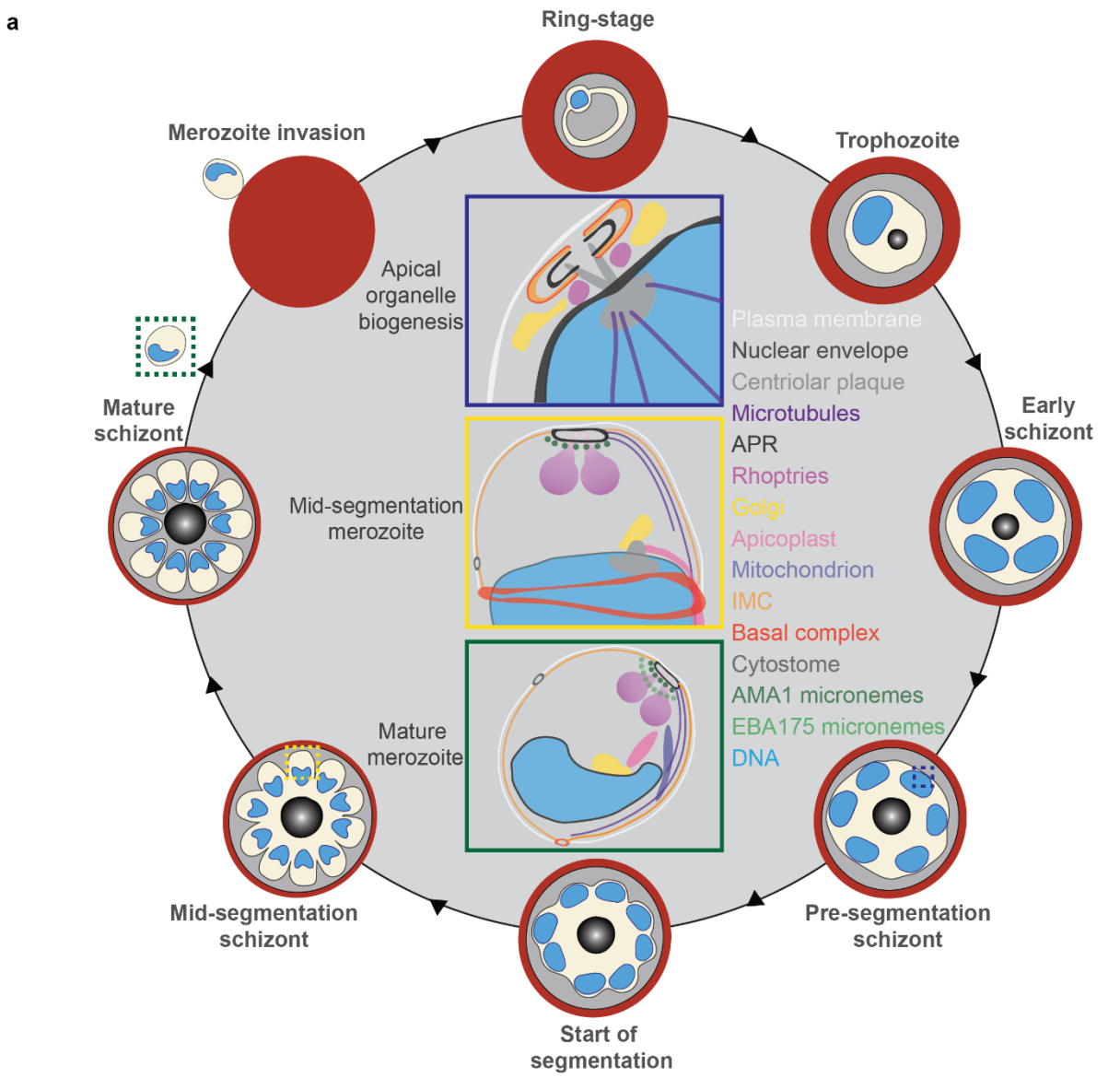
a
Ring-stage
Trophozoite
Early schizont
Pre-segmentation schizont
Start of segmentation
Mid-segmentation schizont
Mature schizont
Merozoite invasion
Apical organelle biogenesis
Mid-segmentation merozoite
Mature merozoite
Plasma membrane
Nuclear envelope
Centriolar plaque
Microtubules
APR
Rhoptries
Golgi
Apicoplast
Mitochondrion
IMC
Basal complex
Cytostome
AMA1 micronemes
EBA175 micronemes
DNA

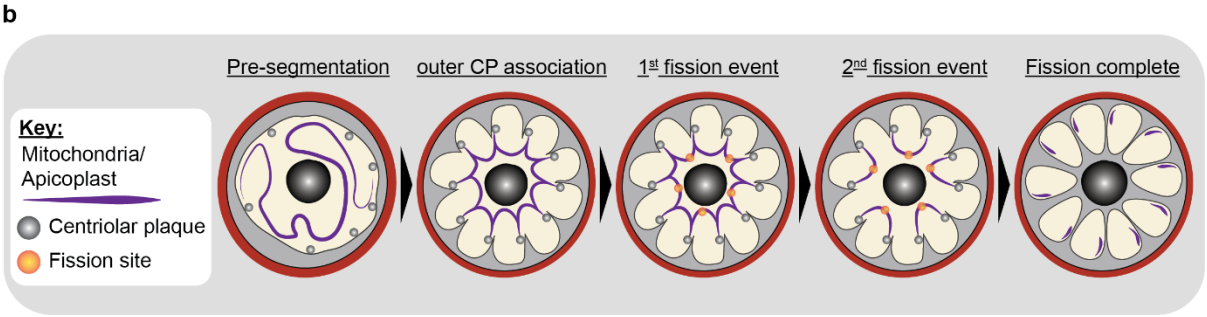
b
Pre-segmentation
outer CP association
1st fission event
2nd fission event
Fission complete
Key:
Mitochondria/ Apicoplast
Centriolar plaque
Fission site